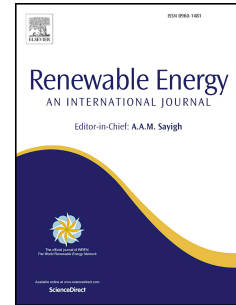


# Journal Pre-proof

A novel three-dimensional numerical model for PV/T water system in hot climate region

Tareq Salameh, Muhammad Tawalbeh, Adel Juaidi, Ramez Abdallah, Abdul-Kadir Hamid



PII: S0960-1481(20)31712-2

DOI: <https://doi.org/10.1016/j.renene.2020.10.137>

Reference: RENE 14427

To appear in: *Renewable Energy*

Received Date: 13 May 2020

Revised Date: 24 October 2020

Accepted Date: 30 October 2020

Please cite this article as: Salameh T, Tawalbeh M, Juaidi A, Abdallah R, Hamid A-K, A novel three-dimensional numerical model for PV/T water system in hot climate region, *Renewable Energy*, <https://doi.org/10.1016/j.renene.2020.10.137>.

This is a PDF file of an article that has undergone enhancements after acceptance, such as the addition of a cover page and metadata, and formatting for readability, but it is not yet the definitive version of record. This version will undergo additional copyediting, typesetting and review before it is published in its final form, but we are providing this version to give early visibility of the article. Please note that, during the production process, errors may be discovered which could affect the content, and all legal disclaimers that apply to the journal pertain.

© 2020 Elsevier Ltd. All rights reserved.

## **A novel three-dimensional numerical model for PV/T water system in hot climate region**

Tareq Salameh<sup>1,\*</sup>, Muhammad Tawalbeh<sup>1</sup>, Adel Juaidi<sup>2,\*</sup>, Ramez Abdallah<sup>2</sup>, Abdul-Kadir Hamid<sup>3</sup>

<sup>1</sup> Sustainable and Renewable Energy Engineering Department, University of Sharjah, P.O. Box 27272, Sharjah, United Arab Emirates

<sup>2</sup> Mechanical Engineering Department- Faculty of Engineering & Information Technology. An-Najah National University, P.O. Box 7, Nablus, Palestine

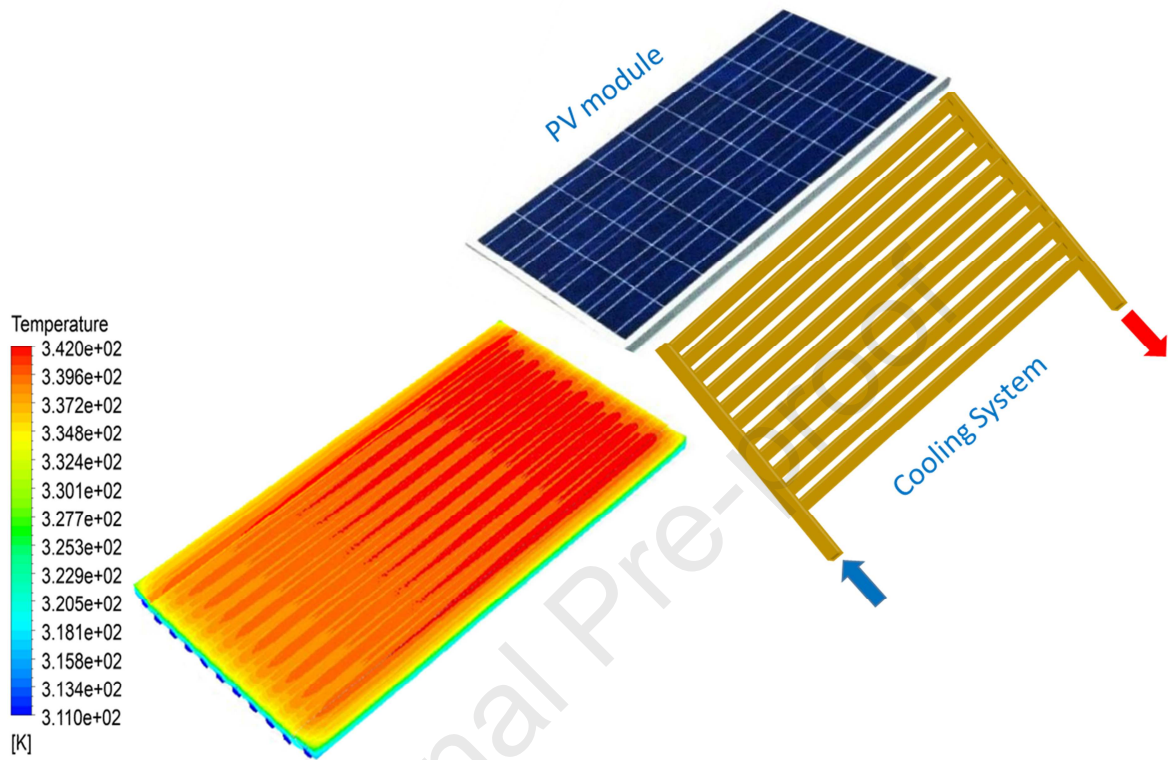
<sup>3</sup> Electrical Engineering Department, University of Sharjah, P.O. Box 27272, Sharjah, United Arab Emirates

\*Corresponding Author: Tareq Salameh, Email: [tsalameh@sharjah.ac.ae](mailto:tsalameh@sharjah.ac.ae)

\*Corresponding Author: \_Adel Juaidi, Email: [adel@najah.edu](mailto:adel@najah.edu)

These two authors contributed equally to this research

## Graphical abstract





19 **Abstract**

20 Hybrid PV/Thermal systems (PV/T) are proposed to harvest the two renewable forms of solar  
21 energy, electrical and thermal. The use of PV/T systems improves electrical efficiency while  
22 utilizing the available solar thermal energy for various heating applications. In this work,  
23 numerical simulations perform for PV/T system in hot climate conditions. The cooling system  
24 consists of eleven channels arranged in parallel to each other on the backside of the PV module.  
25 A novel three-dimensional numerical model of the PV/T system was developed to evaluate the  
26 thermal efficiency. The standard k – epsilon model was used to simulate the flow. This novel  
27 system was based on using symmetric- convection boundary conditions for the right and left  
28 sides of the PV/T model and symmetric-symmetric boundary conditions for the middle cooling  
29 channels rather than simulating the whole cooling system. Using one channel simulation allows  
30 the creation of less number of meshes, hence, reduces the computational time. The thermal  
31 efficiency was estimated by the superposition method for all cooling channels of the PV/T  
32 system. The thermal efficiency of the PV/T system was 60% at 0.4 (L/min) and 68% at 5.4  
33 (L/min). The obtained results were in good agreement with the results presented in the literature.

34

35 **Keywords:** PV/T; Novel numerical model; CFD model simulation; PV cooling; Hot climate

36

37

38

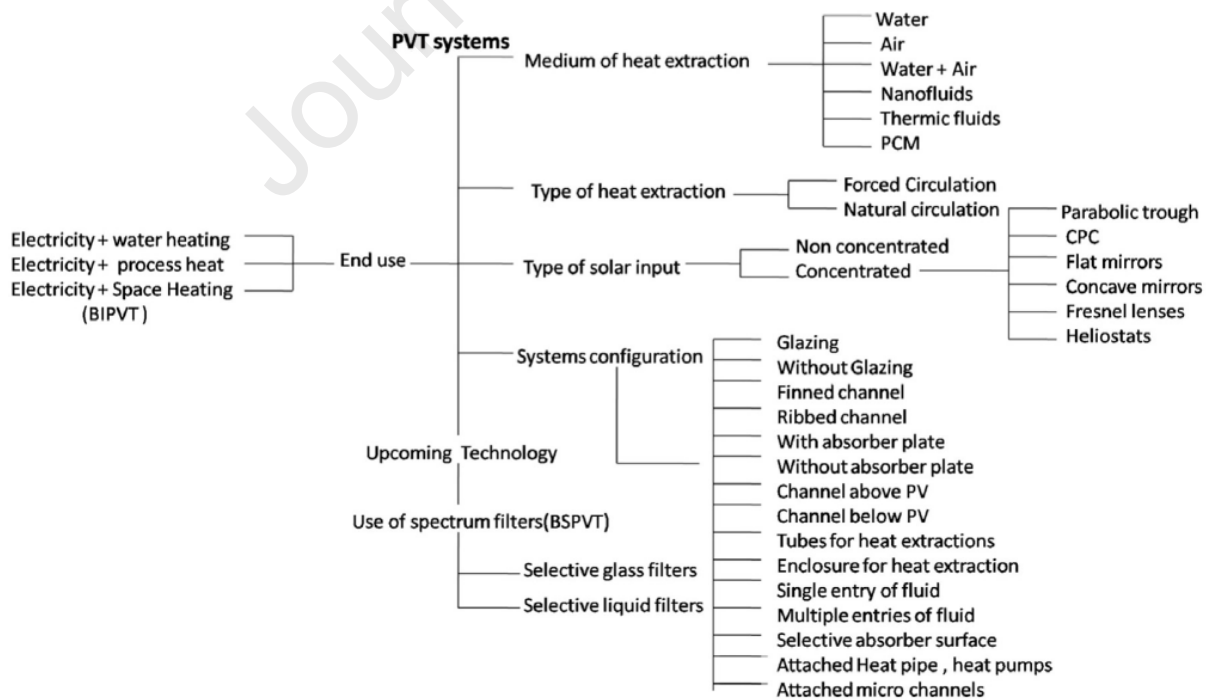
## 39 1. Introduction

40 The increased demand and consumption of fossil fuels led to their fast depletion along with the  
41 elevation of greenhouse gas emissions and consequently, global warming and climate change [1,  
42 2]. The utilization of renewable energy resources and/or the implementation of co-generation  
43 approaches are some favorable alternatives to fossil fuel consumption [3]. Solar energy, in  
44 particular, is not like conventional energy resources that have high environmental impacts. It is a  
45 renewable, abundant, and green source for a sustainable future [4-7].

46 Hybrid PV – Thermal (PV/T) systems that combined photovoltaic (PV) solar cells with solar  
47 thermal absorbers showed significant enhancements in capturing solar energy [8]. Both electrical  
48 and thermal energies are harvested from solar radiation using PV/T hybrid systems. Hence, in  
49 addition to, enhance the electrical efficiency of PV cells, the hybrid system of PV/T will also  
50 capture the thermal energy that can be utilized in various heating applications [9]. This is mainly  
51 because the increase in the PV cell temperature reduces the efficiency of PV cells dramatically  
52 [10]. Nevertheless, the implementation of the PV/T system allows the user to utilize the thermal  
53 energy [11].

54 Several techniques were used for PV cooling such as forced water circulation, forced air  
55 circulation, water spraying, water immersion, heat sink, phase change materials, transparent  
56 cooling, and thermoelectric cooling [12]. Water and air are the most commonly utilized cooling  
57 fluid in PV/T systems [13], where the PV/T system is named according to the cooling fluid  
58 utilized. For instance, PV/T/w and PV/T/a are the water and air-cooled PV/T systems,  
59 respectively. The selection of cooling fluid depends on several aspects and conditions. Using air  
60 as the cooling fluid is simple and cheaper and consequently, more economically feasible.

61 However, it is not efficient in hot climates where air temperatures are above 20°C [14]. On the  
 62 other hand, using water is more efficient, yet, the cooling system would be more expensive when  
 63 compared to the air [15,16]. The utilization of a nanofluid instead of water in a PVT system  
 64 improves the performance and further enhances both electrical and thermal efficiencies [17].  
 65 Illustratively, Nasrin et al. [18] performed experimental and numerical studies for the  
 66 enhancement of the efficiency of the PV/T system using nanofluid based on water/MWCNT for  
 67 different irradiation and MWCT weight fractions. Their results showed that the overall efficiency  
 68 at 1000 W/m<sup>2</sup> irradiance was improved and reached up 89.2%. PV/T systems can be classified in  
 69 accordance with the fluid utilized for cooling, heat extraction type, system configuration  
 70 arrangement, solar input type, and end-use purpose. Figure 1 summarizes the various  
 71 classification of PV/T systems [13].



73

74 **Figure 1:** Classification of PV/T systems [13].

75 United Arab Emirates (UAE) is located in the Arabian Peninsula which is recognized for the hot  
76 and sunny climate throughout the entire year [19]. This substantial exposure to solar radiation  
77 encourages the country to promote photovoltaic technology for electricity generation [20,21]. PV  
78 systems are more environmentally friendly compared to other renewable energy technologies  
79 with no significant operational pollution [22-24] and they require less operating and maintenance  
80 costs [25]. The UAE is one of the highest worldwide countries in electricity consumption, where  
81 the total annual electrical production for Abu Dhabi Water and Electricity Authority (ADWEA)  
82 and Dubai Water and Electricity Authority (DEWA) was approximately 123.0 TWh and the per  
83 capita consumption was around 13.1 MWh [26]. Despite the abundance of oil in UAE, the  
84 country's vision is to include renewable energy and nuclear energy in its energy mix [27]. The  
85 UAE is progressing substantially in achieving its goal by installing several solar power plants  
86 such as SHAMS solar power plant and Mohammed Bin Rashed solar park [28]. Nevertheless, the  
87 UAE hot and dusty weather depresses the performance of solar power systems. For instance,  
88 elevated temperatures [29,30], as well as the accumulation of dust [31,32], negatively affect the  
89 performance of various generations of PV cells. Consequently, the implementation of solar PV  
90 systems in UAE is problematic without proper cooling and cleaning.

91 Nowadays, the electrical efficiency of commercial PV panels ranges from 10 to 25 % [33]. This  
92 means 75 – 90 % of the solar radiation falls on a PV module is either reflected or dissipated as  
93 thermal energy. The latter leads to decreasing the open-circuit voltage and the fill factor of the  
94 module due to the increase in the PV module temperature, hence, decreases the PV module  
95 electrical efficiency [34]. Currently, the most employed PV cells are the monocrystalline silicon

96 (mono c-Si) and the polycrystalline Silicon (poly c-Si) [35]. The efficiencies of these types are  
97 strongly affected by the increase of the panel temperature [34-38], with a temperature coefficient  
98 between  $-0.45$  and  $-0.50\%$  [39]. However, the effect of temperature on the amorphous silicon  
99 cells is significantly lower, with a temperature coefficient of about  $-0.25\%$  [40].

100 Numerous numerical and experimental research investigations have been performed recently to  
101 study, the effect of variation of temperature, irradiation, wind speed, and mass flow rate of the  
102 cooling fluid on the efficiencies of PV/T systems [41-44]. These studies focused mainly on the  
103 overall efficiency of the system, i.e. electrical and thermal efficiencies, and on identifying the  
104 PV/T system that possesses the best performance and the lowest cost. Few studies [43, 45-47]  
105 examined the use of the three-dimensional simulation for the whole PV/T system. The results of  
106 these studies revealed that the thermal efficiency seems to vary with the shape of the cooling  
107 collector, area of PV module, solar irradiance, fluid cooling temperature, overall heat transfer  
108 coefficient, specific heat, and mass flow rate of cooling fluid.

109 The novel numerical model used in this study is based on simulating one cooling channel instead  
110 of simulating the whole PV/T system as reported in other numerical simulations in the literature.  
111 The simulations were performed in this model three times, one time for a cooling channel in the  
112 middle of the PV/T system, one time for the channel on the left side, and one time for the  
113 channel on the right side of the PV/T system. This was achieved by applying symmetric-  
114 symmetric thermal boundary conditions for the channel in the middle and symmetric-convection  
115 thermal boundary conditions for the channels on the left and right sides. It is worthwhile to  
116 mention that the numerical simulations performed for the whole PV/T system require a very high  
117 number of elements and consume more computational time. For instance, the numbers of

118 elements used by Nasrin et al. [43], Pang et al. [45], and Misha et al. [46] were 1,434,582,  
 119 3,262,009, and 2,432,207, respectively. These are 5 to 12 times higher than the number of  
 120 elements used in this study which was 270,000 elements with a computational time of only 7  
 121 minutes. This study aims at numerically studying the performance of a PV/T system using a  
 122 novel three-dimensional model under real conditions of irradiance and temperature for Sharjah  
 123 city, UAE as a semi-arid climate with hot summer and mild winter.

## 124 2. Methodology

### 125 2.1 Electrical part

126 The PV module based on polycrystalline silicon was used, the electrical features of this PV  
 127 module are shown in [48]. The maximum power point ( $P_{MPP}$ ) produced by a solar PV system is  
 128 calculated by Eq. 1:

$$129 \quad \dot{Q}_{MPP} = P_{MPP} = I_{MPP}V_{MPP} = (FF)V_{oc}I_{sc} \quad (1)$$

130 where  $I_{MPP}$  and  $V_{MPP}$  are the current and the voltage at the maximum power point, respectively,  
 131 and  $FF$  is the fill factor that varies from one cell to another. This variation is based on the quality  
 132 of the material used in the cell (purity of silicon). Moreover, the open-circuit voltage and the  
 133 short circuit current are  $V_{oc}$  and  $I_{sc}$ , respectively. The electrical efficiency ( $\eta_{elec}$ ) of the PV  
 134 module is determined using Eq. 2:

$$135 \quad \eta_{elec} = \frac{I_{MPP}V_{MPP}}{GA} \quad (2)$$

136 where  $A$  is the area of the PV module ( $1.17 \text{ m} \times 0.67 \text{ m}$ ), and  $G$  is the irradiance or the solar  
 137 radiation in ( $\text{W}/\text{m}^2$ ). The value of  $MPP$  varies from one location to another based on the ambient

138 temperature and irradiance. The effect of the temperature on the *MPP* is given by temperature  
 139 coefficients for current, voltage, and power. The electrical characteristics of the PV module  
 140 under different conditions are calculated based on the aforementioned coefficients and the  
 141 electrical characteristics under standard test conditions (STC) of the PV module. However, the  
 142 electrical efficiency of the PV module under the effect of the temperature is shown in Eq. 3 [34].

$$143 \quad \eta_{elec} = \eta_{ref} [1 - \beta_{ref}(T - T_{ref})]$$

144 (3)

145 where the  $\eta_{ref}$  is the efficiency at reference temperature,  $\beta_{ref}$  is the temperature coefficient for  
 146 the electrical efficiency,  $T$  is the temperature under actual operating condition (- 40 – 85°C) and  
 147  $T_{ref}$  is the reference temperature under STC (25°C). This drop in efficiency can be reduced by  
 148 using a suitable cooling system to keep the solar module operating close to the SOC.

## 149 2.2 Thermal part

150 The rate of heat removal ( $\dot{Q}_{th}$ ) by the cooling system can be calculated as follows:

$$151 \quad \dot{Q}_{th} = \dot{m}_{water} C_p (T_{outlet} - T_{inlet}) \quad (4)$$

152 where  $\dot{m}_{water}$ ,  $T_{outlet}$ ,  $T_{inlet}$ , and  $C_p$  are the mass flow rate, outlet temperature, inlet temperature,  
 153 and specific heat of the cooling water, respectively. The inlet temperatures were recorded at  
 154 different values of irradiance and. Moreover, the rate of the useful thermal energy ( $\dot{Q}_u$ ) is the  
 155 difference between the rates of absorbed radiation and heat losses and is given by Eq. 5:

$$156 \quad \dot{Q}_u = A_c [G - U_L (T_{p,m} - T_a)]$$

157 (5)

158 where  $A_c$  is the surface area of the collector,  $U_L$  is the overall loss heat transfer coefficient.  $T_{p,m}$ ,  
 159 and  $T_a$  are plate mean temperature and ambient temperature, respectively. However, because of  
 160 the difficulty in measuring  $T_{p,m}$ , Eq. 5 was modified by Hottel and Wilhier [49] to be:

$$161 \quad \dot{Q}_u = A_c F_R [G - U_L (T_{p,m} - T_a)]$$

162 (6)

163 where  $F_R$  is the removal factor and it varies with the incident solar radiation, collector shape  
 164 design, and fluid operating condition as shown in Eq. 7:

$$165 \quad F_R = \frac{\dot{m} C_P}{A_c U_L} \left[ 1 - e^{-\left( \frac{A_c U_L F'}{\dot{m} C_P} \right)} \right]$$

166 (7)

167 Where  $F'$  is the collector efficiency factor. Moreover, the thermal efficiency of the PV/T system  
 168 ( $\eta_{th}$ ) is calculated based on the rate of thermal energy extracted from the PV module as shown in  
 169 Eq. 8:

$$170 \quad \eta_{th} = \frac{\dot{Q}_{th}}{GA} \quad (8)$$

171 Finally, the overall efficiency is the sum of thermal efficiency and electrical efficiency of the  
 172 PV/T system ( $\eta_o$ ) and is calculated as follow:

$$173 \quad \eta_o = \eta_{th} + \eta_{elec} \quad (9)$$

174 One way to improve the efficiency of the PV/T system is to couple it with other heat users such  
 175 as driving a heat pump. This would convert solar energy into useful heat more efficiently and  
 176 increase the working fluid temperature from the combined system significantly, hence, improve  
 177 the overall utilization efficiency of solar energy [50]. However, the coupling adds to the  
 178 complexity of the system and requires additional management due to the instability and  
 179 intermittency nature of solar energy. For instance, during the summer season, the thermal energy  
 180 produced from the combined system could be used to heat the domestic hot water supply, while  
 181 during the winter season an auxiliary heater could be utilized to provide the desired thermal  
 182 energy. Moreover, to attain a steady heating system, the system should be combined with a built-  
 183 in thermal energy storage system such as a reversible thermochemical reaction or a phase change  
 184 material [51]. However, adapting a thermal energy storage system raises the cost of the system  
 185 and introduces more constraints for the system location, therefore, affects the feasibility of the  
 186 whole system [52]. Furthermore, to obtain a more accurate estimate of the PV/T efficiency the  
 187 calculations should be corrected by considering the effect of soiling, energy losses in wires and  
 188 converters, and heat losses in the hydraulic loop [52].

### 189 2.3 Experimental setup and uncertainty

190 The PV/T system consists of a PV module and a thermal system, the specifications of these  
 191 systems are presented in Table 1.

192 **Table 1.** PV/T system specifications.

193

PV/T Components	Specification
PV	Poly-crystalline Si
$P_{\max}$ at STC	100 W

$V_{mp}$	18 V
$I_{mp}$	5.55 A
$V_{oc}$	21.24 V
$I_{sc}$	6,11 A
Operating temperature	- 40 to 85°C
Weight	7.1 kg
Module dimensions	1.17 m × 0.67 m × 0.03 m
<b>Thermal system</b>	
Pump power (DC)	5 W
Pump flow rate	5.4 L/min
Channel material	Copper
Number of channels	11
Channel dimensions	0.0127 m × 0.00635 m
Temperature sensors	- 50 to 250°C
<b>Storage system</b>	
Battery	12 V

194

195 The IV and power curves at different irradiance for the PV module were measured by  
 196 PROFITESTPV. The thermal energy for PV/T system was calculated at different irradiance by  
 197 measuring the mass flow and the inlet and outlet temperatures of the cooling channel as  
 198 presented in Eq. 4. The relative uncertainty for electrical and thermal efficiency were both  
 199 estimated based on the uncertainty associated with the measuring instruments used in the  
 200 experimental setup as shown in Table 2. The absolute uncertainties for measurement parameters  
 201 were estimated based on the instrument device uncertainty and the repetition uncertainty for the  
 202 measured parameter as shown in Eq. 10.

$$203 \quad \delta p = \sqrt{(\delta p_{dev})^2 + (\delta p_{rep})^2} \quad (10)$$

204 where  $\delta p_{dev}$  and  $\delta p_{rep}$  are the device and repetition uncertainties for the measured parameter,  
 205 respectively.

206

207 **Table 2.** Absolute uncertainties for the instrument device and the measured parameter

Instrument device	Measurement variable	Uncertainty	
		Instrument device	Maximum measured
PROFITESTPV (Germany)	Solar irradiance	$\pm 10 \text{ W/m}^2$ for ( $T_{\text{cell}} \pm 1 \text{ K}$ )	$4 \text{ W/m}^2$
PROFITESTPV (Germany)	Peak power	$\pm 5 \text{ W}$	$1 \text{ W}$
Thermocouple type K	Ambient temperature	$\pm 0.5^\circ\text{C}$	$0.3^\circ\text{C}$
TM700 Thermocouple Thermometer	Cooling fluid temperature	$0.1$ to $0.3^\circ\text{C}$	$0.2^\circ\text{C}$
VYAIR 2.4 to 60.0 litres/minute DigiFlow 6710M-66 Digital Micro Flow	Mass flow of cooling fluid	$0.04$ to $0.54 \text{ L/min}$	$0.1 \text{ L/min}$

208

209 If  $R$  is considered as any function of independent linear parameters as in Eq. 11.

$$210 \quad R = f(p_1, p_2, p_3, \dots, p_n) \quad (11)$$

211 Then the absolute uncertainty of function  $R$  can be calculated as follows [53]:

$$212 \quad \delta R = \sqrt{\left(\frac{\partial R}{\partial p_1} \delta p_1\right)^2 + \left(\frac{\partial R}{\partial p_2} \delta p_2\right)^2 + \dots + \left(\frac{\partial R}{\partial p_n} \delta p_n\right)^2} \quad (12)$$

213 where  $n$  is the total number of measured parameters. If the uncertainties of the parameters are214 independent and the absolute uncertainty divided by the function  $R$ , then the absolute uncertainty

215 is converted to relative (fractional) uncertainty as shown in Eq. 13.

$$216 \quad \frac{\delta R}{R} = \sqrt{\left(\frac{\delta p_1}{p_1}\right)^2 + \left(\frac{\delta p_2}{p_2}\right)^2 + \dots + \left(\frac{\delta p_n}{p_n}\right)^2} \quad (13)$$

217 Based on Eq. 13, the uncertainties for electrical and thermal efficiencies were calculated from  
 218 Eqs. 2, 4, and 8 and the values are shown in Table 3.

219

220 **Table 3.** Relative Uncertainties for irradiance, electrical and thermal efficiencies.

$\delta G/G$	$\delta \eta_{elec.}/\eta_{elec.}$	$\delta \eta_{th.}/\eta_{th.}$
$f(G)$ From measurement $\pm 0.0057$	$f(G, P_{MPP.})$ From Eq. (2) $\pm 0.014$	$f(G, \dot{m}_{water}, T_{outlet}, T_{inlet})$ From Eqs. (4) and (8) $\pm 0.02$

221

## 222 2.4 Numerical modeling and simulations

223 3-Dimensional (3-D) numerical simulations were utilized to compute the thermal and hydraulic  
 224 behaviors of the PV/T system. Table 4 shows the physical and thermal properties details of the  
 225 PV module utilized in these simulations [54].

226

227 **Table 4.** Structural details of the PV module used in the simulations [54].

Layer #	Layer name	Thickness (m)	Density (kg/m <sup>3</sup> )	Specific heat capacity (J/kg .K)	Thermal conductivity (W/m.K)
1	ARC	$100 \times 10^{-9}$	2400	691	32
2	Glass	$3 \times 10^{-3}$	3000	500	1.8
3	EVA	$500 \times 10^{-6}$	960	290	0.35

<b>4</b>	PV Cells	$225 \times 10^{-6}$	2330	677	148
<b>5</b>	Rear contact	$10 \times 10^{-6}$	2700	900	237
<b>6</b>	Tedlar	$10 \times 10^{-5}$	1200	1250	0.2

228

229 Figure 2 shows the steady-state energy balance for the PV/T system used in this study. The  
 230 general form for energy balance can be presented as in Eq. 14.

$$231 \quad \frac{dQ}{dt} = \dot{Q}_{in} - \dot{Q}_{out} \quad (14)$$

232 For steady state condition, the previous energy balance equation becomes

$$233 \quad \dot{Q}_{in} = \dot{Q}_{out} \Rightarrow \dot{Q}_{in} = \dot{Q}_{elec} + \dot{Q}_{th} + \dot{Q}_{loss} \quad (15)$$

234 where  $\dot{Q}_{in}$  is the incidence solar irradiance (AG) on the top surface of the PV/T system,  $\dot{Q}_{loss}$  is  
 235 the rate of heat losses from the PV/T system by convection and radiation which are calculated by  
 236 Eqs. 16 and 17, respectively.

$$237 \quad \dot{Q}_{conv} = h A_c (T_{p,m} - T_a) \quad (16)$$

$$238 \quad \dot{Q}_{rad} = \sigma \varepsilon (T_{p,m} + T_{sky}) (T_{p,m}^2 + T_{sky}^2) A_c (T_{p,m} - T_{sky}) \quad (17)$$

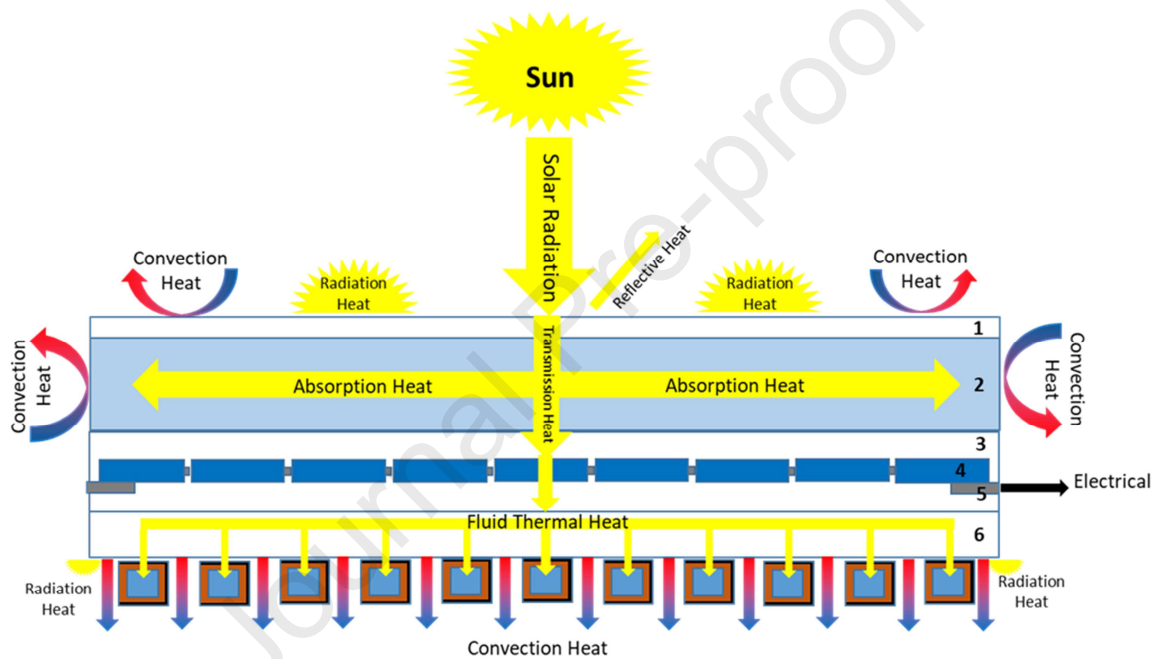
239 where  $h$  is the heat transfer coefficient in (W/m<sup>2</sup>.K), for this condition,  $h$  was used based on the  
 240 approximation proposed by Watmuff et al. 1977 [55].

$$241 \quad h = 2.8 + 3 \times V \quad (18)$$

242 where  $V$  is the speed of wind in (m/s). This approximation is used after considering the variation

243 on the speed is less than 4 (m /s).  $\sigma$  is Stefan Boltzmann constant which equal to  $5.67 \times 10^{-8}$   
 244  $\text{W/m}^2 \cdot \text{K}^4$ ,  $\varepsilon$  is the emissivity of the PV/T surface and  $T_{sky} = 0.0552T_a^{1.5}$  is the sky temperature  
 245 [43]. The solar PV system was cooled from the backside, the copper channel dimensions are  
 246  $0.0127 \text{ m} \times 0.00635 \text{ m}$ .

247



248

249 **Figure 2.** The energy balance for a PV/T system consists of eleven copper cooling channels.

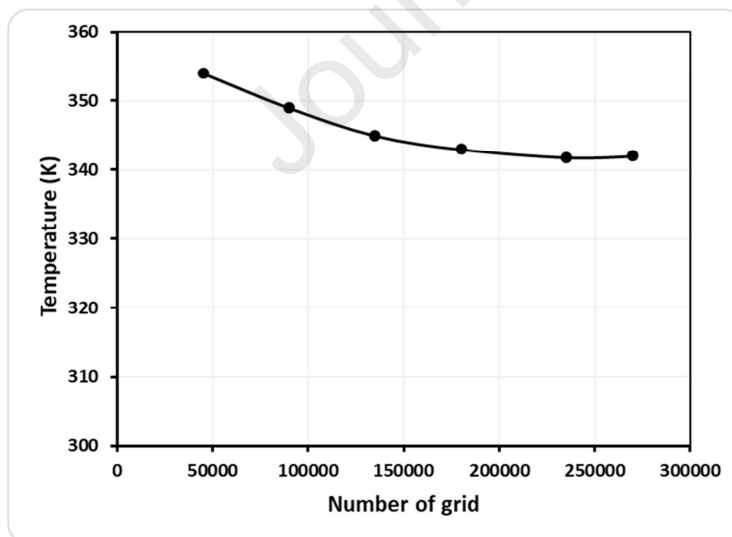
250

### 251 2.4.1 Geometry and mesh

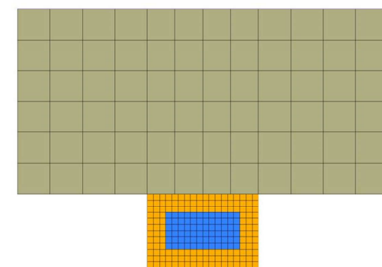
252 The geometry was created in 3-D by DesignModeler software inside ANSYS 15. The geometry  
 253 was split into several control volumes to solve for conservation equations. The hexahedral  
 254 shaped elements were used for simulations because it has a high aspect ratio as shown in Figure

255 3. The mesh size was selected based on grid independent study. The mesh size was refined for  
 256 the fluid flow inside the cooling channel, the size was 0.00071 m. However, the size for the mesh  
 257 inside the PV module was 0.0032 m as shown in Figure 3. Different numbers of grids were  
 258 tested and the average temperature at the middle of the top surface was selected for the grid  
 259 independent study as shown in Figure 3. The numerical uncertainty in the fine-grid for this CFD  
 260 simulation was estimated by 2.37 % based on the study done by [56]. In order to reduce the time  
 261 of computational and achieve the convergence quickly, only one cooling channel out of eleven  
 262 channels is considered in the numerical simulation instead to discretized the whole geometry of  
 263 the PV/T system (PV module and the thermal system which consist from eleven copper cooling  
 264 channels).

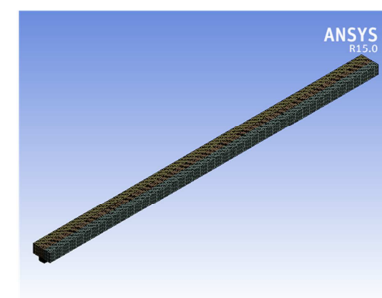
265



(a)



(b)



(c)

266

267 **Figure 3:** (a) Effect of the number of grids on the temperature at the top of PV module (b) Cross

268 section along the stream wise direction with hexahedral elements shapes for PV/T model (c)  
269 Computational domain of the PV/T numerical model with a copper cooling channel at the bottom  
270 with 270000 hexahedral elements.

271

#### 272 **2.4.2 Physical properties and boundary conditions**

273 The equivalent thermo-physical properties for the structural details of the PV module were used  
274 as in [57] after assumed the PV module one homogeneous unit. The values of these thermo-  
275 physical properties were based on the information displayed in Table 4 and Figure 2, while the  
276 thermo-physical properties for copper channels and the working fluid were used from the  
277 ANSYS Fluent database. The solar irradiance received the top surface of the computational  
278 domain was treated as constant heat flux after considering the product of solar transmissivity and  
279 solar absorptivity ( $\tau\alpha$ ) of the PV module 0.9 [58], these values of heat flux were  $900 \text{ W/m}^2$ ,  $700$   
280  $\text{W/m}^2$ , and  $550 \text{ W/m}^2$  at different times of a typical day in April as shown in [48]. Both inlet and  
281 outlet boundary conditions were applied to the inlet and outlet positions of the copper cooling  
282 channel, respectively; four inlet water velocity values were simulated based on 0.4, 1.4, 3.4, and  
283 5.4 (L/min) as the total mass flow rate in all eleven channels.

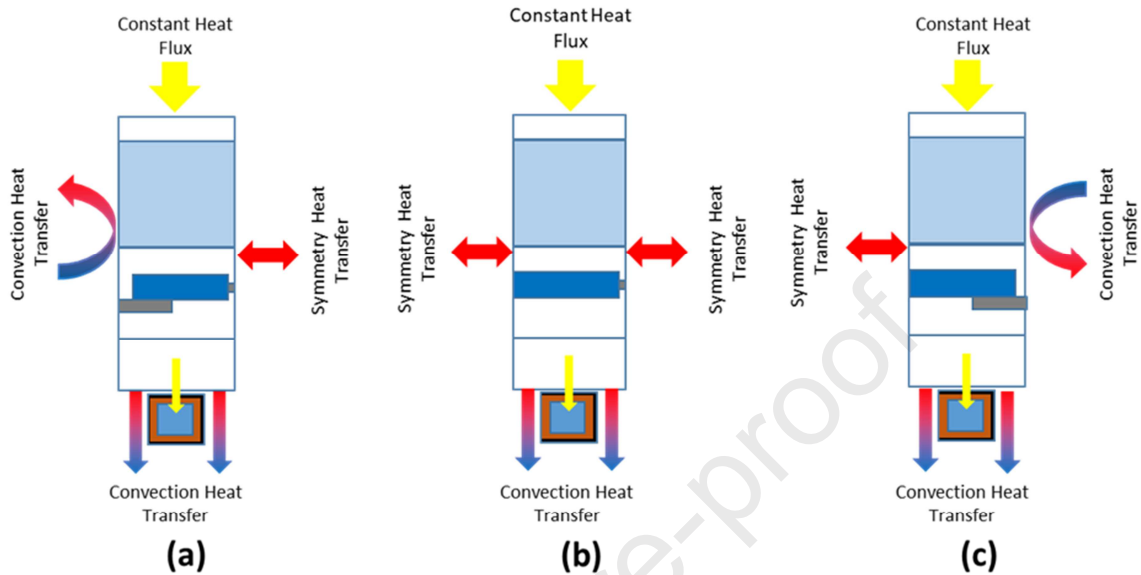
284 The convective heat transfer boundary condition was applied at the upper and lower side edges  
285 of the PV/T numerical model, as well as at the bottom side of the PV/T numerical model (PV  
286 module part) as shown in Figure 4. Two different thermal boundary conditions were applied on  
287 both sides (left and right) of the PV/T numerical model based on the position of the cooling  
288 channel as mentioned before. The symmetric boundary condition was used for the cooling

289 channel located in the middle of the PV module, while both symmetric and convective thermal  
 290 boundaries condition were used for the cooling channel located at the left and right sides of the  
 291 PV module. It is worth mentioning that the insulation thermal condition was applied to the  
 292 copper cooling channel walls. The details of the boundary conditions for each type of PV/T  
 293 model are presented in Table 5 and Figure 4.

294 **Table 5.** Type of boundary condition for three different locations of PV/T numerical model.

Location of PV/T system	Type of boundary condition for different locations of PV/T numerical model		
	Right side	Middle	Left side
Top of PV module	Constant heat flux (500, 700, and 900 W/m <sup>2</sup> )	Constant heat flux (500, 700, and 900 W/m <sup>2</sup> )	Constant heat flux (500, 700, and 900 W/m <sup>2</sup> )
Right side of PV module	Convection heat transfer	Symmetry	Symmetry
Left side of PV module	Symmetry	Symmetry	Convection heat transfer
Bottom side of PV module	Convection and radiation heat transfer	Convection and radiation heat transfer	Convection and radiation heat transfer
Upper side edge of PV module	Convection and radiation heat transfer	Convection and radiation heat transfer	Convection and radiation heat transfer
Lower side edge of PV module	Convection and radiation heat transfer	Convection and radiation heat transfer	Convection and radiation heat transfer
Inlet of copper channel	Constant velocity temperature, kinetic energy and dissipation rate	Constant velocity temperature, kinetic energy and dissipation rate	Constant velocity temperature, kinetic energy and dissipation rate
Outlet of copper channel	Pressure outlet	Pressure outlet	Pressure outlet
Inner walls of copper channel	No slip for velocity	No slip for velocity	No slip for velocity
	Convection for temperature	Convection for temperature	Convection for temperature
Outer wall of copper channel	Thermal insulation	Thermal insulation	Thermal insulation

295



296

297 **Figure 4.** Boundary conditions for three different locations of PV/T model (a) left (b) middle (c)  
 298 right.

299

### 300 2.4.3 Governing equations and mathematical model

301 ANSYS Fluent was used the finite volume method to solve the steady-state governing equations

302 for the PV/T numerical model as shown in Table 6.

303

304

305

306

307 **Table 6.** Steady-state governing equations for the  $k$ - $\varepsilon$  turbulence model.
$$\left\{ \frac{\partial}{\partial x} (\rho u \phi) + \frac{\partial}{\partial y} (\rho v \phi) + \frac{\partial}{\partial z} (\rho w \phi) \right\} = \frac{\partial}{\partial x} \left( \Gamma_\phi \frac{\partial \phi}{\partial x} \right) + \frac{\partial}{\partial y} \left( \Gamma_\phi \frac{\partial \phi}{\partial y} \right) + \frac{\partial}{\partial z} \left( \Gamma_\phi \frac{\partial \phi}{\partial z} \right) + S_\phi$$

Equation	$\phi$	$\Gamma_\phi$	$S_\phi$
Continuity	1	0	0
$U$ momentum	$u$	$\mu + \mu_t$	$-\frac{\partial p}{\partial x} + \frac{\partial}{\partial x} \left( \Gamma_\phi \frac{\partial u}{\partial x} \right) + \frac{\partial}{\partial y} \left( \Gamma_\phi \frac{\partial v}{\partial x} \right) + \frac{\partial}{\partial z} \left( \Gamma_\phi \frac{\partial w}{\partial x} \right)$
$V$ momentum	$v$	$\mu + \mu_t$	$-\frac{\partial p}{\partial y} + \frac{\partial}{\partial x} \left( \Gamma_\phi \frac{\partial u}{\partial y} \right) + \frac{\partial}{\partial y} \left( \Gamma_\phi \frac{\partial v}{\partial y} \right) + \frac{\partial}{\partial z} \left( \Gamma_\phi \frac{\partial w}{\partial y} \right)$
$W$ momentum	$w$	$\mu + \mu_t$	$-\frac{\partial p}{\partial z} + \frac{\partial}{\partial x} \left( \Gamma_\phi \frac{\partial u}{\partial z} \right) + \frac{\partial}{\partial y} \left( \Gamma_\phi \frac{\partial v}{\partial z} \right) + \frac{\partial}{\partial z} \left( \Gamma_\phi \frac{\partial w}{\partial z} \right)$
Temperature	$T$	$\mu/Pr + \mu_t/Pr_t$	0
Turbulent kinetic energy	$k$	$\mu + \mu_t/\sigma_k$	$G_k - \rho\varepsilon$
Dissipation rate	$\varepsilon$	$\mu + \mu_t/\sigma_\varepsilon$	$C_{1\varepsilon} \frac{\varepsilon}{k} G_k - \rho C_{2\varepsilon} \frac{\varepsilon^2}{k}$

308

309  $G_k$  is the generation of turbulence kinetic energy due to the mean velocity gradients and is given

310 by Eq. 19.

$$311 \quad G_k = -\overline{\rho u'_i u'_j} \frac{\partial u_j}{\partial x_i} \quad (19)$$

312 The variables  $\sigma_k$  and  $\sigma_\varepsilon$  are the turbulent Prandtl numbers for  $k$  and  $\varepsilon$ .  $C_{1\varepsilon}$  and  $C_{2\varepsilon}$  are313 constants. The values of  $\sigma_k$ ,  $\sigma_\varepsilon$ ,  $C_{1\varepsilon}$ , and  $C_{2\varepsilon}$  were 1, 1.3, 1.44, and 1.92, respectively. The

314 turbulent viscosity is calculated by combining  $k$  and  $\varepsilon$  as in Eq. 20.

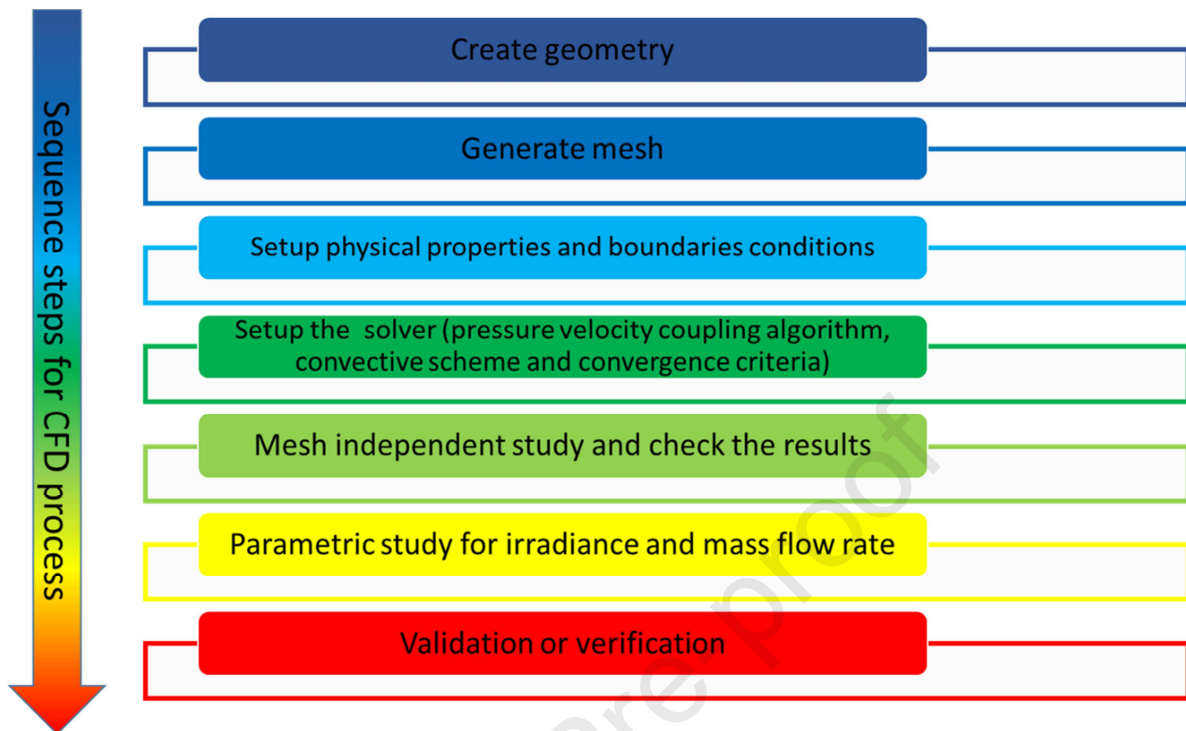
$$315 \quad \mu_t = \rho C_\mu \frac{k^2}{\varepsilon} \quad (20)$$

316 The modeling constants  $C_\mu$  value is 0.09. Both mass and Navier–Stokes equations were used to  
 317 solve the incompressible flow field for the  $k$ - $\varepsilon$  turbulence model inside the copper cooling  
 318 channel, while the energy equation was used to solve the temperature fields for the flow field  
 319 inside the copper cooling channel, copper channel walls and the PV module. The convergence  
 320 criteria for mass, momentum, and energy equations were  $10^{-4}$ ,  $10^{-6}$ , and  $10^{-7}$ , respectively, these  
 321 convergence criteria achieved after 7 minutes. The outlet temperature was evaluated based on  
 322 the area average weight of the outlet of the cooling channel as shown in Eq. 21.

$$323 \quad T_{out} = \frac{1}{T_{out}} \int T_{out} dA \quad (21)$$

324 After the outlet temperature of cooling fluid was evaluated, Eq. 4 was used to calculate the  
 325 thermal energy for the PV/T numerical model for the two cooling channels at the right and left  
 326 (symmetric-convection) as well as the nine cooling channels at the middle (symmetric-  
 327 symmetric) of PV/T system. Figure 5 shows the diagram for all procedures needed for the CFD  
 328 of the PV/T system numerical simulations in this study.

329



330

331 **Figure 5.** The methodology adopted for numerical simulations of the PV/T system using  
 332 ANSYS Fluent.

333

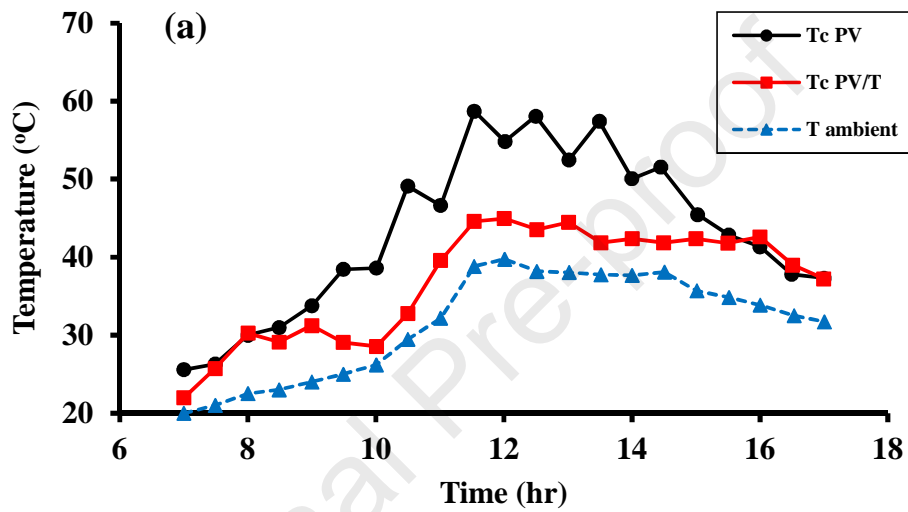
### 334 3. Results and Discussion

#### 335 3.1 Weather conditions

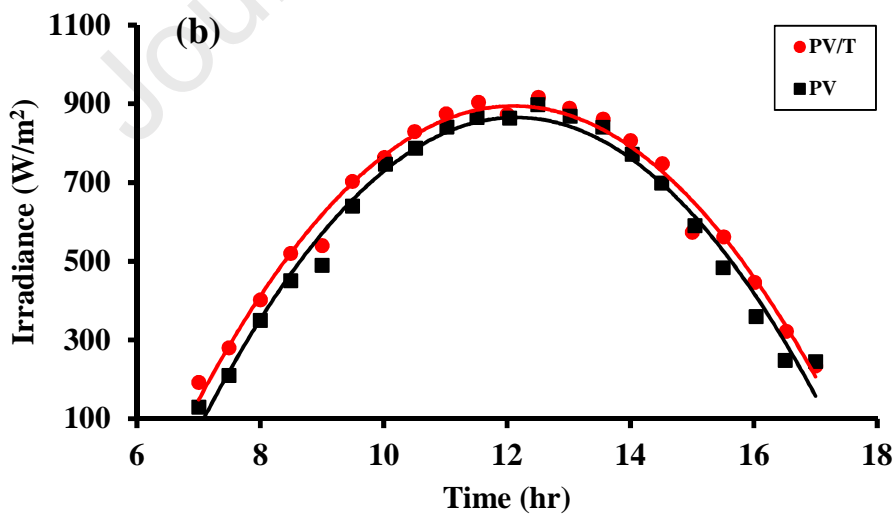
336 Figures 6 (a) and (b) display the ambient temperature, cell temperature, and the irradiance for  
 337 both PV and PV/T modules during a typical day in April for Sharjah city in UAE. All the  
 338 temperature curves in Figure 6 (a) follow the natural distribution of the ambient temperature  
 339 during daylight. These three temperatures increase with time and reach a maximum values at  
 340 around noon. These maximum temperature values for both PV/T and PV modules are 45 and

341 58°C, respectively, at maximum ambient temperature of 40°C. Then the temperatures decrease  
 342 gradually until sunset. On the other hand, Figure 6 (b) shows that the irradiance for both PV and  
 343 PV/T modules reaches maximum values of 916 and 898 W/m<sup>2</sup>, respectively, at the solar noon.

344



345



346

347 **Figure 6:** The measuring parameters for PV and PV/T modules during a typical day of April in  
348 UAE (a) Ambient temperature and cell temperatures for PV and PV/T (b) Irradiance falls on PV  
349 and PV/T modules.

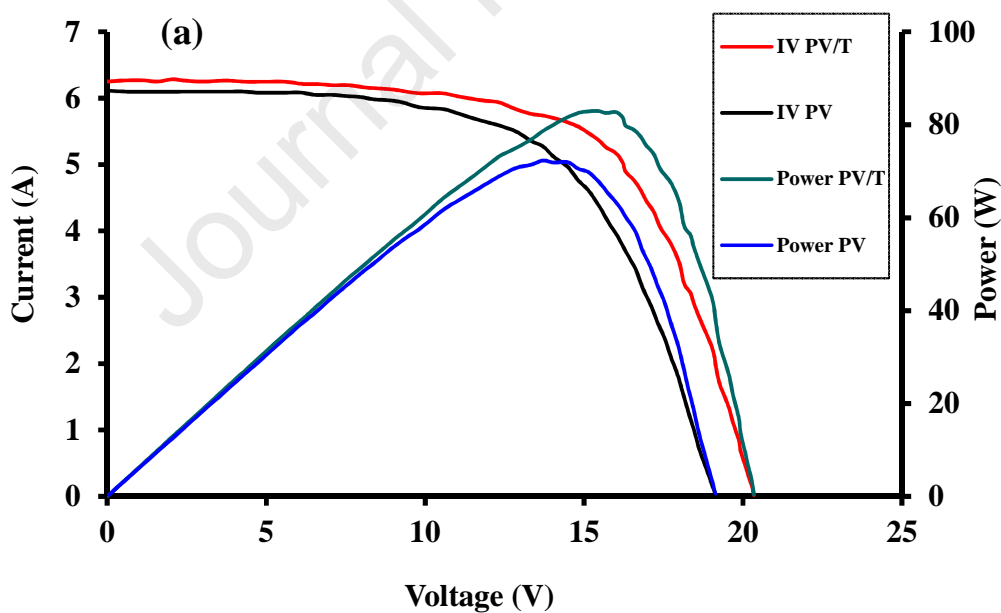
350

### 351 3.2 Electrical characteristic for the PV and PV/T systems

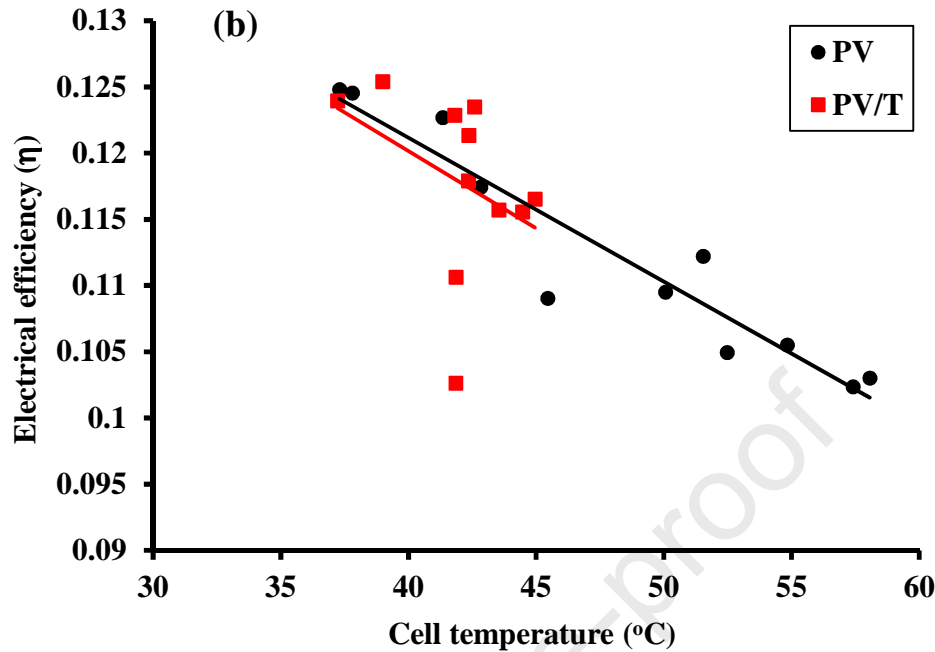
352 The electrical characteristics of the PV and the PV/T systems were measured using the profiTest  
353 PV analyzer device under three values of irradiance namely at 12:30 PM ( $900 \text{ W/m}^2$ ) as shown  
354 in Figure 7 (a). It is clear from this figure that the PV/T module has a higher open-circuit voltage  
355 value of 20.34 V compared to the PV module value of 19.12 V. Whereas the values for the short  
356 circuit current were 6.25 A and 6.11 A for the PV/T and PV modules, respectively. The PV/T  
357 module shows a maximum power point (MPP) value of 82.97 W, the MPP for the PV/T is higher  
358 than the value of MPP for the PV module by 10 W. Figure 6 shows the measurements of  
359 electrical efficiencies for the PV/T and PV modules under different values of irradiance  
360 measured on the same working day in April. These efficiencies decrease linearly as the PV cell  
361 temperature increases as illustrated in Figure 7 (b). It is evident from Figure 6 that the minimum  
362 and maximum measurement electrical efficiencies for the PV/T module were 10.26 % and 12.5  
363 %, respectively. On the other hand, the minimum and maximum measurement electrical  
364 efficiencies for the PV module were 10.23 % and 12.5, respectively. It is clear that there was no  
365 difference between the upper and lower limits of the electrical efficiencies and that is mainly due  
366 to the narrow range of the cell temperatures of the PV/T module ( $37.22 - 44.95^\circ\text{C}$ ). This makes  
367 the cooling system for the PV/T module more effective compared to the PV module without the  
368 cooling where the cell temperature ranges between  $37.3$  and  $58.06^\circ\text{C}$ . This difference in cell

369 temperature causes the 10 W increase in the MPP as aforementioned. The drop in the cell  
370 temperature enhances electrical efficiency, especially under hot climate weather conditions. In  
371 other words, the cell temperature for the PV/T was very close to the nominal operating cell  
372 temperature (NOCT) or the standard operating conditions (SOC), which allows the PV/T system  
373 to operate at a higher electrical efficiency compared to the PV system. The latter works at a cell  
374 temperature far away from the SOC temperature. The cooling system extracted the waste heat  
375 during the energy conversion process. Furthermore, the cooling system will enhance the overall  
376 efficiency of PV/T by recovery this wasted thermal energy and make the system more  
377 sustainable.

378



379



380

381 **Figure 7:** The electrical performance for PV and PV/T system during a typical day in April in  
 382 UAE (a) The IV and power curves (b) Electrical efficiency.

383

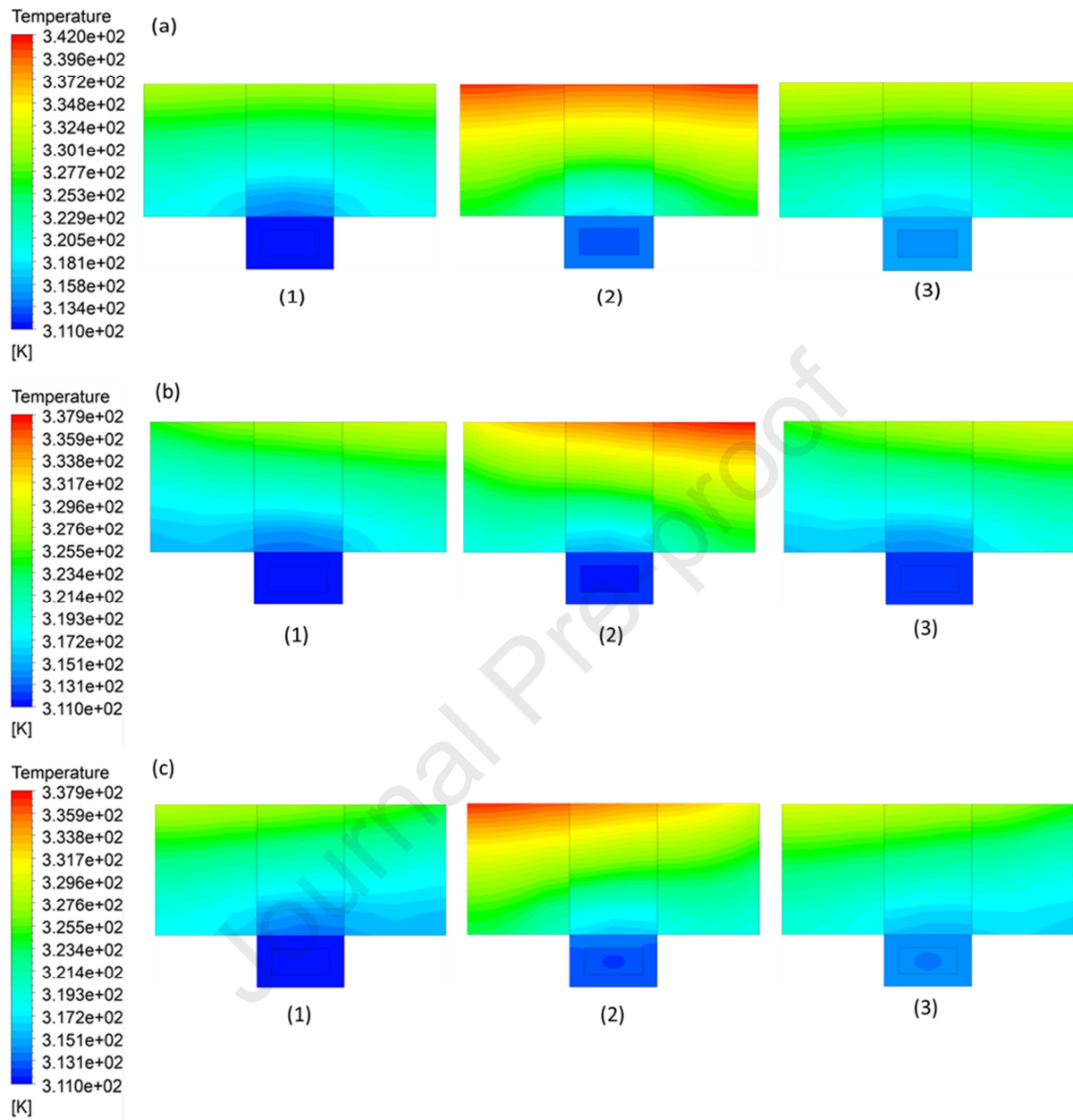
### 384 3.3 Thermal characteristics of the PV/T system

#### 385 3.3.1 Two-dimensional temperature distribution

386 The two-dimensional temperature distribution for PV/T system along the cooling channel (at the  
 387 inlet, middle, and outlet positions) is displayed in Figure 8. As shown in Figure 8 (a), the value  
 388 of the highest temperature was 342 K which was observed on the top surface in the middle of the  
 389 PV/T module. This was when the symmetrical boundary condition applied on both sides in the  
 390 numerical model. However, the lowest temperature was 311 K and it was at the inlet of the

391 cooling channel. The temperature on the top surface of the PV/T module for the symmetrical  
392 boundary condition decreases along the cooling channel from inlet to outlet. The range of the  
393 temperatures on the top surface were 311 to 330.1 K, 313.4 to 342 K, and 315.8 to 334.8 K for  
394 the inlet, middle, and outlet location of the cooling channel, respectively. While Figure 8 (b) and  
395 (c) show the two-dimensional temperature distribution when the symmetrical and convective  
396 boundaries conditions applied on both sides of the numerical model. The highest temperature  
397 was 337.9 K and it was observed in the middle of the PV/T module. The value of temperature for  
398 this boundary condition is lower than the value when the symmetrical thermal boundary  
399 condition applied on both sides of the numerical model. By similarity with symmetrical  
400 boundary conditions, the temperature at the top side of the PV/T module decreases along the  
401 cooling channel from inlet to outlet. The ranges of temperature in the inlet, middle, and outlet  
402 locations on the top surface were 311 to 327.6 K, 311 to 337.9 K, and 311 to 329.6 K,  
403 respectively. Figures 8 (a), (b), and (c) show also that the top side of the PV/T module has the  
404 highest value of the temperature where the constant heat flux is applied, this value decreases to  
405 the lowest value when reaches the bottom of the copper channel of the cooling system.

406



407

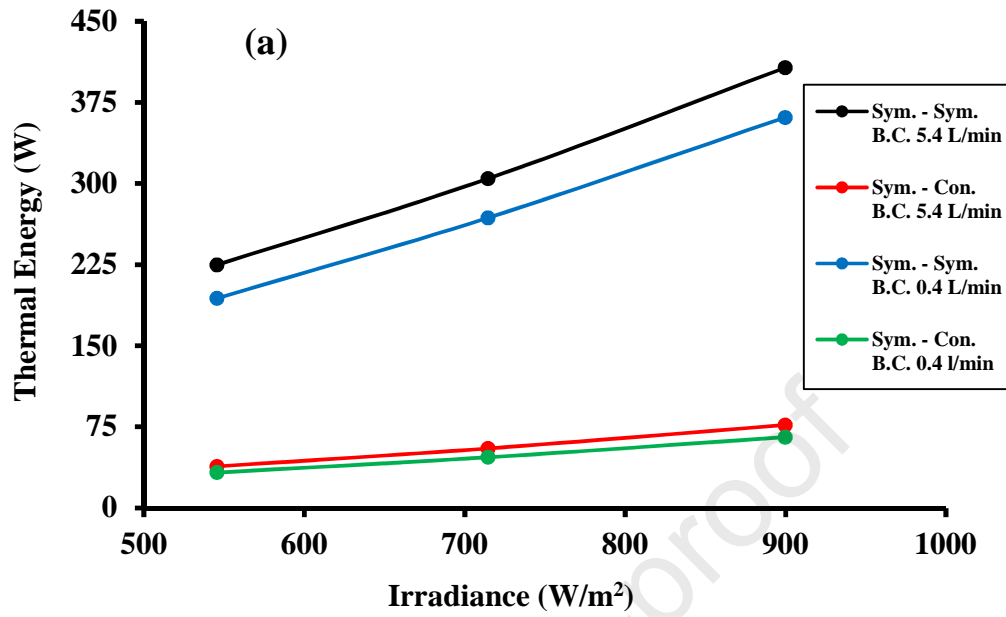
408 **Figure 8:** Temperature contour plot for different boundary condition (a) symmetric-symmetric  
 409 along the middle of PV module length (b) symmetric-convection conditions along the right edge  
 410 of the PV module length (c) symmetric-convection conditions along the left edge of the PV  
 411 module length at different location (1) inlet (2) middle (3) outlet.

### 412 3.3.2 Useful thermal energy from the PV/T system

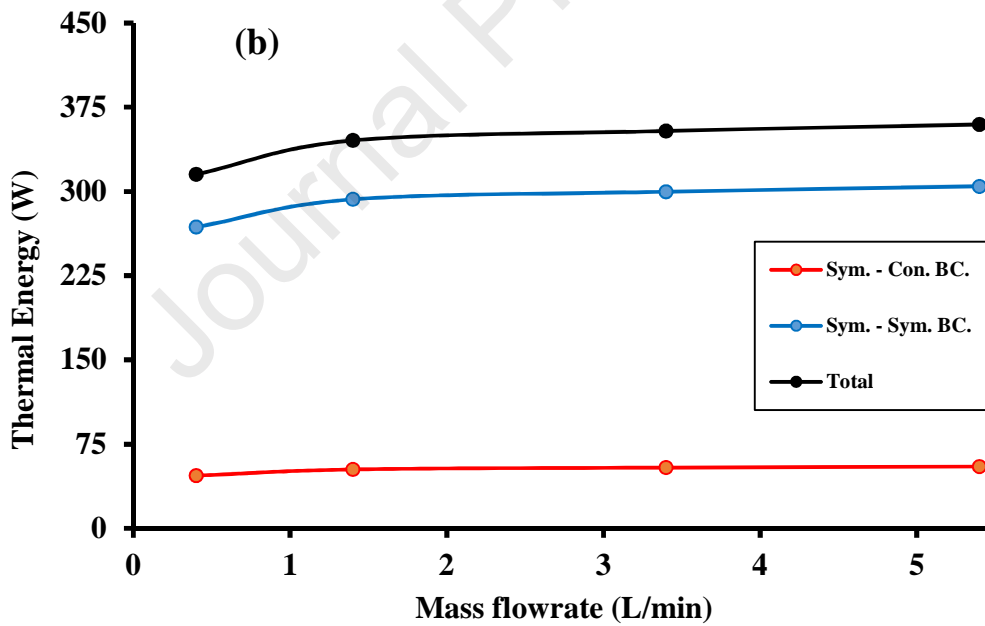
413 Figure 9 (a) shows the useful thermal energy of the PV/T that was absorbed by water under  
414 different values of irradiance (550, 700, and 900 W/m<sup>2</sup>). The absorbed thermal energy increases  
415 as both irradiance and mass flow rates increase from 500 to 900 W/m<sup>2</sup> and from 0.4 to 5.4 L/min,  
416 respectively. Corresponding to what mentioned in Figure 8, the thermal energy is higher when  
417 symmetrical boundary conditions applied on both sides of the PV/T module for the channels  
418 located in the middle of the PV/T module. It is worth it to point out that nine channels out of  
419 eleven have symmetrical thermal boundary conditions (Sym. - Sym. B.C.) on both sides of the  
420 PV/T numerical model. While the channel on the left side edge of the PV/T module has  
421 convection and symmetrical (Conv. - Sym. B.C.) thermal boundary conditions on the left and  
422 right sides edges of the PV/T numerical model, respectively, and vice versa for the right side  
423 edge of the PV/T module. The thermal energy variation with all values of mass flow rates for  
424 different thermal boundary conditions at 700 W/m<sup>2</sup> is shown in Figure 9 (b). The thermal energy  
425 for both boundary conditions increases as the mass flow rates increase from 0.4 to 5.4 L/min.  
426 The big variation of thermal energy with the mass flow rates is clearly obtained for the channel  
427 in the middle of the PV/T module at the low mass flow rate as compared to the two channels on  
428 the left and right edges of the PV/T module. The total thermal energy for the PV/T model will  
429 follow the trend of thermal energy for symmetrical- symmetric boundary conditions, that  
430 because this boundary condition applied for the majority of channels (9 channel out of 11).

431

432



433



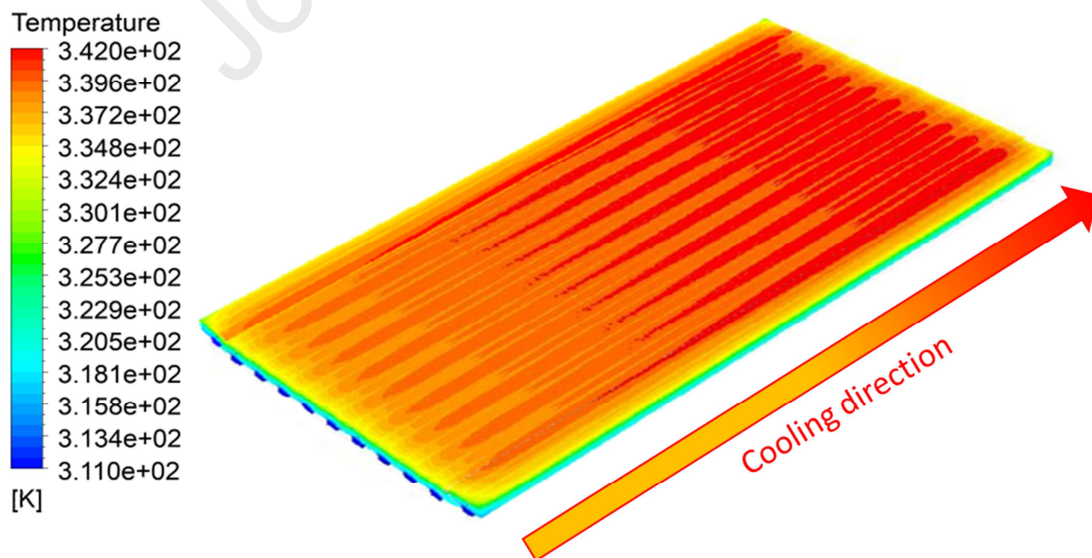
434

435 **Figures 9:** Thermal energy under different thermal boundary conditions (a) different irradiance436 values along the day (b) different mass flow rates values at 700 W/m<sup>2</sup>.

### 437 3.3.3 Three-dimensional temperature distribution

438 Figure 10 shows the three-dimensional temperature distribution for the PV/T module. The  
 439 temperature readings have the highest value at the upper surface where the PV/T module  
 440 exposed to constant irradiance (heat flux). The temperature on the top surface increases along the  
 441 direction of the cooling from the inlet at 334.8 K to 342 K in the middle then tends to decrease  
 442 again to 337.2 K at the outlet. The figure shows also the effect of symmetric-symmetric and  
 443 symmetric convection boundary conditions on the temperature values. All the edges around the  
 444 top side of the PV/T module, especially at the corners, where the symmetric convection  
 445 boundary conditions applied have the lowest temperatures. The temperature of the PV/T module  
 446 decreases from 334.8 - 342 K at the top surface to around 327.7 K at the middle plane between  
 447 the top and bottom surfaces. The temperature reaches the lowest value of 311 K at the bottom  
 448 surface where the water cooling channels installed.

449



450

451

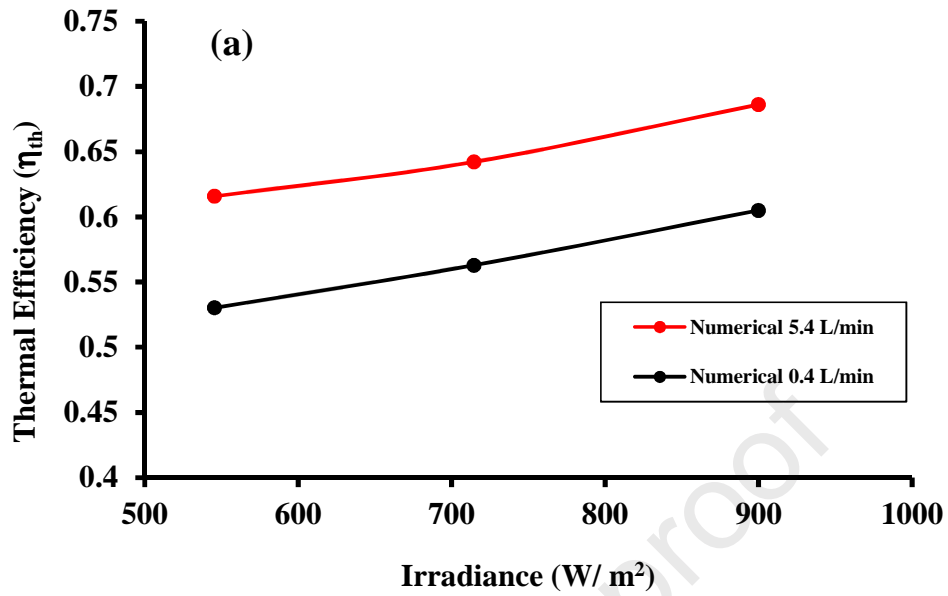
452 **Figure 10:** Three-dimensional temperature distribution in (K) for PV/T system for a typical day  
453 in April in UAE.

454

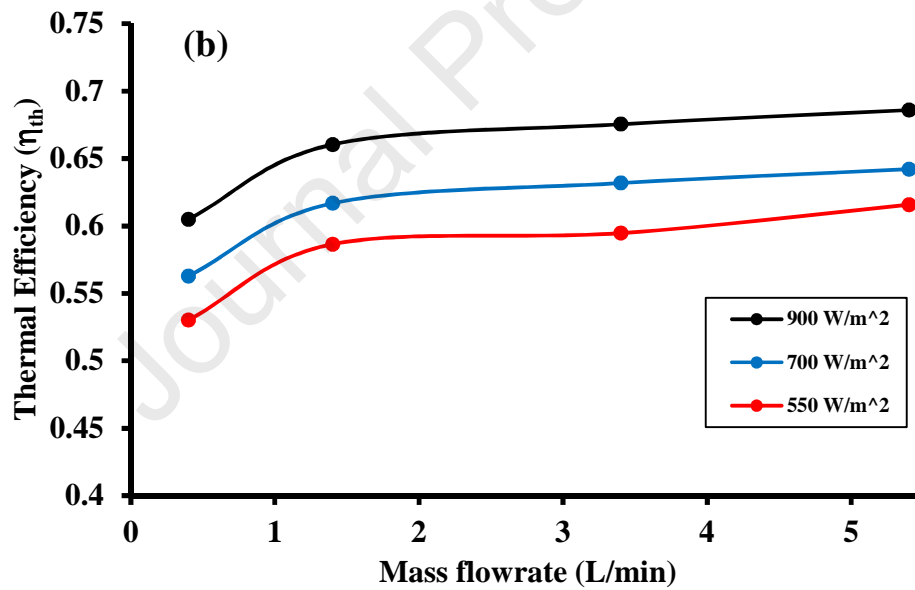
### 455 3.3.4 Thermal efficiency of the PV/T system

456 The thermal efficiency under different irradiance and mass flow rates are displayed in Figure 11  
457 (a) and (b). Evidently, the thermal efficiency increases as the irradiance increase under the same  
458 mass flow rate, the mass flow rate 5.4 L/min has a higher thermal efficiency value than the mass  
459 flow rate 0.4 L/min, where the maximum  $\eta_{th}$  obtained at 900 ( $W/m^2$ ) as displayed in Figure 11  
460 (a). Figure 11 (b) shows the variation of the thermal efficiency with the mass flow rate. For 900  
461  $W/m^2$ , as the mass flow rate increases from 0.4 to 1.4 L/min the thermal efficiency increases  
462 from 61% to 66%. After that, it increases slightly from 66% to 69% as the mass flow rate  
463 increases from 1.4 to 5.4 L/min. It is noteworthy to mention that the feasible value of the mass  
464 flow rate in this study is 1.4 L/min. The feasible value of the mass flow rate is crucial for  
465 selecting the capacity of the pump which is an essential factor for the cost-effectiveness of the  
466 PV/T cooling system.

467



468



469

470 **Figures 11:** Thermal efficiency for a typical day of April in UAE at (a) different irradiance

471

values along the day (b) different values of mass flow rates.

472

### 473 3.3.5 Validation and verification of the current PV/T model

474 The results of the thermal efficiency for this work were compared with several studies in the  
475 literature. For example, the numerical simulation of this work was performed for three different  
476 values of irradiance (500, 700, and 900 W/m<sup>2</sup>) and four different mass flow rates (0.4, 1.4, 3.4,  
477 and 5.4 L/min). The removal factor  $F_R(\tau\alpha)$  is the maximum efficiency that the PV/T module can  
478 achieve when  $\Delta T/G$  equals zero, i.e. intersection of the vertical axis for  $\eta_{th}$  versus  $\Delta T/G$ . The  
479  $F_R(\tau\alpha)$  computed from this numerical model was very close to the value reported in Sandnes et  
480 al. 2002 [59] at 5.4 (L/min). Moreover, the  $F_R U_L$  values have small differences due to the  
481 difference in the area of the PV module, evident from Figure 12 (a) and Table 7. Furthermore,  
482 the values of  $F_R(\tau\alpha)$  and  $F_R U_L$  reported in Sandnes et al. 2002 [59] depend on the weather  
483 conditions. On the other hand, the values of  $F_R(\tau\alpha)$  and  $F_R U_L$  computed by the developed model  
484 at a low mass flow rate (0.4 and 1.4 L/min) were compared to the values reported in Tiwari et al.  
485 2006 [58], Zondag et al. 2003 and 2002 [60,61] and Tripanagnostopoulos et al. 2002 [62], see  
486 Figure 12 (b) and Table 2. However, the small difference in the values of  $F_R U_L$  is due to the  
487 difference in the PV module area and the high thermal conductivity of the copper cooling  
488 channel. It is evident from Table 2 that the values of  $F_R U_L$  for this work were high at low mass  
489 flow rates and were low at high mass flow rates.

490 Table 7 shows a summary of the results reported in the literature [58, 59 - 62] for  $F_R(\tau\alpha)$  and  
491  $F_R U_L$  compared to the results obtained in this work for different PV/T module areas. The results  
492 reported in the literature were based on experimental work or numerical models of one, two, or  
493 three dimensional. Figure 12, on the other hand, shows a comparison between the thermal  
494 efficiency in this study and various studies in the literature under varying values of  $\Delta T/G$  for

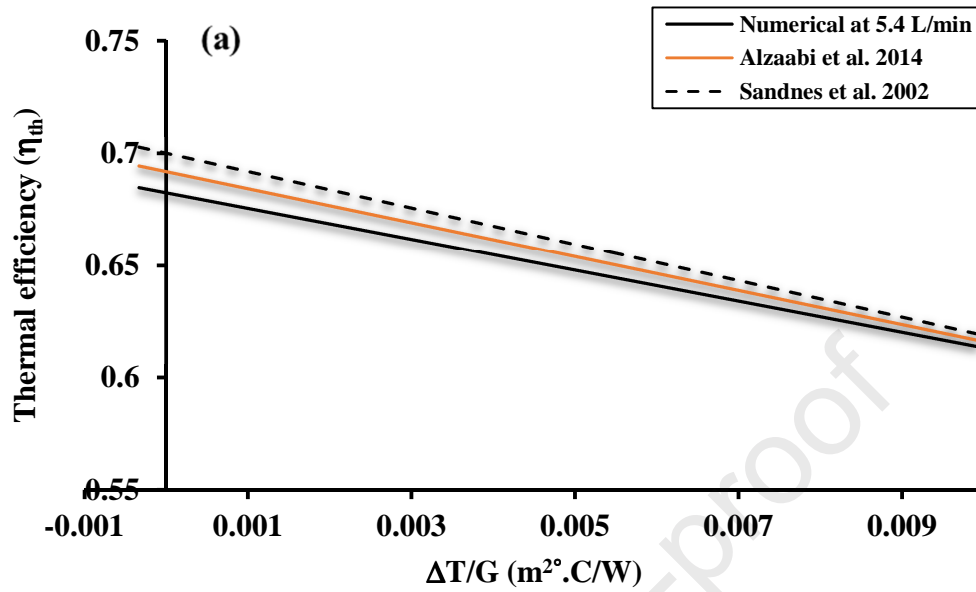
495 high and low mass flow rates. It is clear from Figure 9 that the thermal efficiency is inversely  
 496 proportional to  $\Delta T/G$  for all studies. It is worth it to mention that the highest thermal efficiency  
 497 obtained at different values of the mass flow rate [63-69], and the covered or glazed PV/T has  
 498 less thermal efficiency compared with the uncovered or unglazed [59, 60]. Moreover, in addition  
 499 to mass flow rate value, the highest value of thermal efficiency for the PV/T system depends on  
 500 many parameters such as ambient, operating conditions, the spacing between the channels, and  
 501 the area of PV/T module as shown in Eqs. 6 and 7.

502

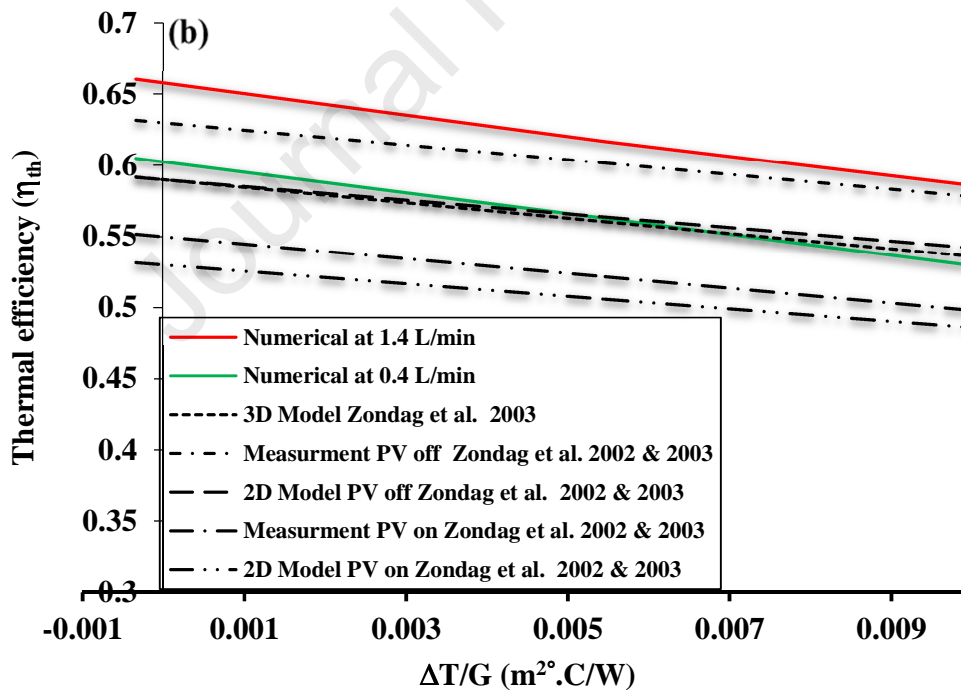
503 **Table 7.** Summary of thermal efficiency parameters (intersection  $FR(\tau\alpha)$ , and slope  $FRU_L$ ) for  
 504 the current work and other studies in the literature.

$\eta_{th \text{ at } \Delta T/G = 0} (\%) \text{ or } FR(\tau\alpha)/\text{average}$	$FRU_L$ (W/m <sup>2</sup> .C)	Area (m <sup>2</sup> )	Mass flow rate (Unit)	Irradiance (W/m <sup>2</sup> )	Reference
0.70	8.10	0.32	-	-	[59]
0.6825	6.89	0.784	5.4 L/min		[This study]
0.72	8.50	0.32	-	-	[59]
0.6825	6.89	0.784	5.4 L/min		[This study]
0.58 (m PV off)	5.2	0.94	76 kg/m <sup>2</sup> h	800	[60]
0.63 (2D PV off)	4.8				
0.6575	7.24	0.784	1.4 L/min	550, 700	[This study]

0.53 (m PV on)	5.2			and 900	
0.55 (2D PV on)	4.4				
0.625 / 0.56 (1D)	5.4	0.94	0.02 kg/s	800	<b>[61]</b>
0.62 / 0.535 (2D)	4.8				
0.59 (3D)					
0.6575	7.24	0.784	1.4 L/min	550, 700 and 900	<b>[This study]</b>
0.71	9.04	0.4	0.02 kg/s	850.910, 898	<b>[22]</b>
0.6575	7.24	0.784	1.4 L/min	550, 700 and 900	<b>[This study]</b>
77.25		0.648	45 kg	Winter	<b>[58]</b>
60 – 65					
60.3 – 65.8	7.27	0.784	0.4 – 1.4 L/min	Summer	<b>[This study]</b>



506



507

508 **Figures 12:** Comparison of experimental and numerical thermal efficiency versus  $\Delta T/G$  (a) at

509 5.4 L/min with work done by [39,44] (b) at 0.4 &amp; 1.4 L/min with work done by [45,46].

510

511 **4. Conclusions**

512 Novel 3-D numerical simulations were performed under different irradiance conditions and mass  
513 flow rates to study the performance of the PV/T system. The computational time for numerical  
514 simulation was reduced by applying different thermal boundary conditions on both sides of the  
515 novel PV/T numerical model. The number of elements for the numerical simulations conducted  
516 in the literature was higher than the current study by 5 to 12 times which lead to an increase in  
517 the computational time. The current model is much simpler and more efficient with less  
518 computational time. The results demonstrate that the middle of the PV/T module has the highest  
519 temperature where the symmetrical boundary conditions were applied on both sides of the PV/T  
520 numerical model. Several factors, namely, the overall heat transfer coefficient, the mass flow  
521 rate, the area of PV module, the specific heat, and the ambient conditions (irradiance, ambient,  
522 and fluid cooling temperature) affect the thermal efficiency of the PV/T system. A low value of  
523  $(\Delta T/G)$  has the highest thermal efficiency where the irradiance and the temperature difference  
524 between the ambient temperature and the inlet temperature of the cooling fluid were very high  
525 and very low, respectively. The novel numerical model shows that these results were in a decent  
526 concurrence with the results reported in the literature. The overall efficiency enhanced not only  
527 by increasing the electrical efficiency from 1 to 1.5 % but also by utilizing the thermal energy for  
528 some applications such as solar heating and cooling systems. As in solar liquid desiccant cooling  
529 system for trigeneration applications (cooling, heating, and power generation), solar desiccant  
530 wheel evaporative cooling system (SDWECS), adsorption gas heat pump, and domestic hot  
531 water. There are several limitations for this model such as the cooling channels were distributed

532 in a symmetrical configuration, the cooling channels should be rectangular and fixed at the  
533 backside of the PV module, the contact region between the PV module and the cooling channels  
534 was assumed to be perfect without any resistance, the flow is incompressible and turbulent, and  
535 the variation on the wind speed is less than 4 m/s.

536

537 **Acknowledgement:** The authors would like to acknowledge the: University of Sharjah and An  
538 Najah National University for facilitating this research.

539

#### 540 **References**

541 [1] A. Ahmadi, M. El Haj Assad, D. H. Jamali, R. Kumar, Z. X.Li, T. Salameh, M. Al-Shabi, M.  
542 A. Ehyaei, Applications of geothermal organic Rankine Cycle for electricity production, Journal  
543 of Cleaner Production 274 (2020) 122950.

544 [2] A.H. Alami, A. Abu Hawili, M. Tawalbeh, R. Hasan, L. Al Mahmoud, S. Chibib, A.  
545 Mahmood, K. Aokal, P. Rattanapany, Materials and logistics for carbon dioxide capture, storage  
546 and utilization, Science of The Total Environment 717 (2020) 137221.

547 [3] C. Ghenai, T. Salameh, A. Merabet, Technico-economic analysis of off grid solar PV/Fuel  
548 cell energy system for residential community in desert region, International Journal of Hydrogen  
549 Energy 45 (2020) 11460-11470.

- 550 [4] A. Juaidi, F.G. Montoya, J.A. Gázquez, F. Manzano-Agugliaro, An overview of energy  
551 balance compared to sustainable energy in United Arab Emirates. *Renewable and Sustainable*  
552 *Energy Reviews* 55 (2016) 1195-1209.
- 553 [5] R. Abdallah, A. Juaidi, S. Abdel-Fattah, F. Manzano-Agugliaro, Estimating the Optimum Tilt  
554 Angles for South-Facing Surfaces in Palestine, *Energies*, 13(3) (2020) 623;  
555 DOI:10.3390/en13030623
- 556 [6] M. A. Ehyaei, A. Ahmadi, M. El Haj Assad, Tariq Salameh, Optimization of parabolic  
557 through collector (PTC) with multi objective swarm optimization (MOPSO) and energy, exergy  
558 and economic analyses, *Journal of Cleaner Production* 234 (2019) 285-296.
- 559 [7] C. Ghenai, A. Merabet, T. Salameh, E.C. Pigem, Grid-tied and stand-alone hybrid solar  
560 power system for desalination plant, *Desalination* 435 (2018) 172-180.
- 561 [8] C. Ghenai, T. Salameh, A. Merabet, A.K. Hamid, Modeling and optimization of hybrid solar-  
562 diesel-battery power system. 2017 7th International Conference on Modeling, Simulation, and  
563 Applied Optimization (ICMSAO): IEEE; (2017). p. 1-5.
- 564 [9] M. Farshchimonfared, J.I. Bilbao, A.B. Sproul, Channel depth, air mass flow rate and air  
565 distribution duct diameter optimization of photovoltaic thermal (PV/T) air collectors linked to  
566 residential buildings, *Renewable Energy* 76 (2015) 27-35.
- 567 [10] A.H. Alami, K. Aokal, D. Zhang, M. Tawalbeh, A. Alhammadi, A. Taieb, Assessment of  
568 Calotropis natural dye extracts on the efficiency of dye-sensitized solar cells, *Agronomy*  
569 *Research* 16 (2018) 1569-1579.

- 570 [11] F. Schiro, A. Benato, A. Stoppato, N. Destro, Improving photovoltaics efficiency by water  
571 cooling: Modelling and experimental approach, *Energy*, 137, (2017), 798-810.
- 572 [12] J. Siecker, K. Kusakana, B.P. Numbi, A review of solar photovoltaic systems cooling  
573 technologies, *Renewable and Sustainable Energy Reviews* 79 (2017) 192-203.
- 574 [13] S.S. Joshi, A.S. Dhoble, Photovoltaic -Thermal systems (PVT): Technology review and  
575 future trends, *Renewable and Sustainable Energy Reviews* 92 (2018) 848-882.
- 576 [14] C. Lamnatou, D. Chemisana, Photovoltaic/thermal (PVT) systems: A review with emphasis  
577 on environmental issues, *Renewable Energy* 105 (2017) 270-287.
- 578 [15] M.S. Buker, B. Mempo, S.B. Riffat, Performance evaluation and techno-economic  
579 analysis of a novel building integrated PV/T roof collector: An experimental validation, *Energy*  
580 *and Buildings* 76 (2014) 164-175.
- 581 [16] F. Yazdanifard, E. Ebrahimi-Bajestan, M. Ameri, Investigating the performance of a  
582 water-based photovoltaic/thermal (PV/T) collector in laminar and turbulent flow regime,  
583 *Renewable Energy* 99 (2016) 295-306.
- 584 [17] E. Bellos, C. Tzivanidis, Yearly performance of a hybrid PV operating with nanofluid,  
585 *Renewable Energy* 113 (2017) 867-884.
- 586 [18] R. Nasrin, N.A. Rahim, H. Fayaz, M. Hasanuzzaman, Water/MWCNT nanofluid based  
587 cooling system of PVT: Experimental and numerical research, *Renewable Energy* 121 (2018)  
588 286-300.

- 589 [19] A. Aldawoud, T. Salameh, Y. K. Kim, Double skin façade: energy performance in the  
590 United Arab Emirates, *Energy Sources, Part B: Economics, Planning, and Policy*, (2020)  
591 DOI.org/10.1080/15567249.2020.1813845
- 592 [20] T. Salameh, M. El Haj Assad, M. Tawalbeh, C. Ghenai, A. Merabet, H. F.Öztop, Analysis  
593 of cooling load on commercial building in UAE climate using building integrated photovoltaic  
594 façade system, *Solar Energy*199 (2020) 617-629.
- 595 [21] T. Salameh, C. Ghenai, A. Merabet, M. Alkasrawi, Techno-economical optimization of an  
596 integrated stand-alone hybrid solar PV tracking and diesel generator power system in  
597 Khorfakkan, United Arab Emirates, *Energy* 190 (2020) 116475.
- 598 [22] M.M. Aman, K.H. Solangi, M.S. Hossain, A. Badarudin, G.B. Jasmon, H. Mokhlis, A.H.A.  
599 Bakar, S.N Kazi, A review of Safety, Health and Environmental (SHE) issues of solar energy  
600 system, *Renewable and Sustainable Energy Reviews* 41 (2015) 1190-1204.
- 601 [23] A.H. Alami, M. Faraj, K. Aokal, A.A. Hawili, M. Tawalbeh, D. Zhang, Investigating  
602 various permutations of copper iodide/FeCu tandem materials as electrodes for dye-sensitized  
603 solar cells with a natural dye, *Nanomaterials* 10 (4) (2020) 784; DOI: 10.3390/nano10040784.
- 604 [24] T. Salameh, M. Tawalbeh, A.H. Alami, A. Al-Othman, S. Issa, M. Alkasrawi, Life Cycle  
605 Analysis Comparison between Single Crystalline Solar Cells and poly Crystalline Gallium in  
606 UAE. 2020 *Advances in Science and Engineering Technology International Conferences*  
607 (ASET): Dubai, United Arab Emirates (2020) 1-6. DOI: 10.1109/ASET48392.2020.9118328.

- 608 [25] P. Bhubaneswari, S. Iniyar, R. Goic, A review of solar photovoltaic technologies,  
609 Renewable and Sustainable Energy Reviews 15 (2011) 1625-1636.
- 610 [26] V. Eveloy, T. Gebreegziabher, Excess electricity and power-to-gas storage potential in the  
611 future renewable-based power generation sector in the United Arab Emirates, Energy 166 (2019)  
612 426-450.
- 613 [27] M. Tawalbeh, T. Salameh, M. Albawab, A. Al-Othman, M.E.H. Assad, A.H. Alami,  
614 Parametric study of a single effect lithium bromide-water absorption chiller powered by a  
615 renewable heat source, Journal of Sustainable Development of Energy, Water and Environment  
616 Systems 8 (2020) 464-475.
- 617 [28] A. Al-Othman, M. Tawalbeh, M. El Haj Assad, T. Alkayyali, Ahmed Eisa, Novel multi-  
618 stage flash (MSF) desalination plant driven by parabolic trough collectors and a solar pond: A  
619 simulation study in UAE, Desalination 443 (2018) 237-244.
- 620 [29] V. Perraki, G. Tsolkas, Temperature dependence on the photovoltaic properties of selected  
621 thin-film modules, International Journal of Renewable and Sustainable Energy 2 (2013) 140-146.
- 622 [30] M. Berginc, U.O. Krasovec, M. Jankovec, and M. Topic, The effect of temperature on the  
623 performance of dye-sensitized solar cells based on a propyl-methyl- imidazolium iodide  
624 electrolyte, Solar Energy Materials & Solar Cells 91 (2007) 821-828.
- 625 [31] M. Mani, R. Pillai, Impact of dust on solar photovoltaic (PV) performance: Research status,  
626 challenges and recommendations, Renewable and Sustainable Energy Reviews 14 (2010) 3124-  
627 3131.

- 628 [32] F. Mejia, J. Kleissl, J.L. Bosch, The effect of dust on solar photovoltaic systems, Energy  
629 Procedia 49 (2014) 2370-2376.
- 630 [33] M.A. Green, S.P. Bremner, Energy conversion approaches and materials for high-efficiency  
631 photovoltaics, Nature Materials 16 (2017) 23-34.
- 632 [34] E. Skoplaki, J.A. Palyvos, On the temperature dependence of photovoltaic module electrical  
633 performance: A review of efficiency/power correlations, Solar Energy 83 (2009) 614-624.
- 634 [35] R. Kumar, M.A. Rosen, A critical review of photovoltaic–thermal solar collectors for air  
635 heating, Applied Energy 88 (2011) 3603-3614.
- 636 [36] S. Chander, A. Purohit, A. Sharma, S.P. Nehra, M.S. Dhaka, Impact of temperature on  
637 performance of series and parallel connected mono-crystalline silicon solar cells, Energy Reports  
638 1 (2015) 175-180.
- 639 [37] M. Al-Chaderchi, K. Sopian, T. Salameh, D. Zhang, M. Alghoul, Enhancing the  
640 Performance of PV Panel Undergoing Shading Effects, International Journal of Power  
641 Electronics and Drive Systems 9 (2018) 937-1943.
- 642 [38] M. Al-chaderchi, K. Sopian, M. Alghoul, T. Salameh, Experimental study of the effect of  
643 fully shading on the Solar PV module performance. E3S Web of Conferences: EDP Sciences;  
644 (2017) p. 01001.
- 645 [39] A.K. Tossa, Y.M. Soro, L. Thiaw, Y. Azoumah, L. Sicot, D. Yamegueu, C. Lishou, Y.  
646 Coulibaly, G. Razongles, Energy performance of different silicon photovoltaic technologies  
647 under hot and harsh climate, Energy 103 (2016) 261-270.

- 648 [40] S.A. Kalogirou, Y. Tripanagnostopoulos, Hybrid PV/T solar systems for domestic hot water  
649 and electricity production, *Energy Conversion and Management* 47 (2006) 3368-3362.
- 650 [41] P. Ooshaksaraei, K. Sopian, S.H. Zaidi, R. Zulkifli, Performance of four air-based  
651 photovoltaic thermal collectors configurations with bifacial solar cells, *Renewable Energy* 102  
652 (2017) 279-293.
- 653 [42] O. Rejeb, H. Dhaou, A. Jemni, A numerical investigation of a photovoltaic thermal (PV/T)  
654 collector, *Renewable Energy* 77 (2015) 43-50.
- 655 [43] R. Nasrin, M. Hasanuzzaman, N.A. Rahim, Effect of high irradiation and cooling on power,  
656 energy and performance of a PVT system, *Renewable Energy*, 116, (2018), 552-569.
- 657 [44] A.H.A. Al-Waeli, M.T. Chaichan, K. Sopian, H.A. Kazem, H.B. Mahood, A.A. Khadom,  
658 Modeling and experimental validation of a PVT system using nanofluid coolant and nano-PCM,  
659 *Solar Energy* 177 (2019) 178-191.
- 660 [45] W. Pang, Q. Zhang, Y. Cui, L. Zhang, H. Yu, X. Zhang, Y. Zhang, H. Yan, Numerical  
661 simulation and experimental validation of a photovoltaic/ thermal system based on a roll-bond  
662 aluminum collector, *Energy* 187 (2019) 115990.
- 663 [46] S. Misha, A.L. Abdullah, N. Tamaldin, M.A.M. Rosli, F.A. Sachit, Simulation CFD and  
664 experimental investigation of PVT water system under natural Malaysian weather conditions,  
665 *Energy Reports*, (2019) In press. (<https://doi.org/10.1016/j.egy.2019.11.162>).
- 666 [47] T. Salameh, M. Tawalbeh, A. Juaidi, R. Abdallah, S. Issa and A. H. Alami, A novel  
667 numerical simulation model for the PVT water system in the GCC region, 2020 *Advances in*

- 668 Science and Engineering Technology International Conferences (ASET): Dubai, United Arab  
669 Emirates (2020) pp. 1-5, doi: 10.1109/ASET48392.2020.9118264.
- 670 [48] A.A. Alzaabi, N.K. Badawiyeh, H.O. Hantoush, A.K. Hamid, Electrical/thermal  
671 performance of hybrid PV/T system in Sharjah, UAE, International Journal of Smart Grid and  
672 Clean Energy 3 (2014) 385 – 389.
- 673 [49] C.C. Smith, T.A. Weiss, Design application of the Hottel-Whillier-Bliss equation, Solar  
674 Energy 19 (2) (1977) 109 – 113.
- 675 [50] J. Yao, H. Xu, Y. Dai, M. Huang, Performance analysis of solar assisted heat pump coupled  
676 with build-in PCM heat storage based on PV/T panel, Solar Energy 197 (2020) 279–291.
- 677 [51] J. Yao, W. Liu, Lu Zhang, Binshou Tian, Yanjun Dai, Mingjun Huang, Performance  
678 analysis of a residential heating system using borehole heat exchanger coupled with solar  
679 assisted PV/T heat pump, Renewable Energy 160 (2020) 160-175
- 680 [52] L. de Santoli, G.L. Basso, B. Nastasi, The Potential of Hydrogen Enriched Natural Gas  
681 deriving from Power-to-Gas option in Building Energy Retrofitting, Energy and Buildings 149  
682 (2017) 424–436.
- 683 [53] S.J. Kline, F.A. McClintock, Describing uncertainties in single-sample experiments. Mech.  
684 Eng. 75 (1953) 3-8.
- 685 [54] D.J. Yang, Z.F. Yuan, P.H. Lee, H.M. Yin, Simulation and experimental validation of heat  
686 transfer in a novel hybrid solar panel, International Journal of Heat and Mass Transfer 55 (2012)  
687 1076–1082.

- 688 [55] J.H. Watmuff, W.W.S. Charters, D. Proctor, Solar and wind induced external coefficients -  
689 Solar collectors, Cooperation Mediterranee pour l'Energie Solaire, Revue Internationale  
690 d'Helio-technique, 2nd Quarter, 1977, p. 56.
- 691 [56] I.B. Celik, U. Ghia, P.J. Roache, C.J. Freitas, Procedure for Estimation and Reporting of  
692 Uncertainty Due to Discretization in CFD Applications, ASME. J. Fluids Eng. July 2008;  
693 130(7): 078001.
- 694 [57] S. Armstrong, W.G. Hurley, A thermal model for photovoltaic panels under varying  
695 atmospheric conditions, Applied Thermal Engineering 30 (2010) 1488-1495.
- 696 [58] A. Tiwari, M.S. Sodha, Performance evaluation of hybrid PV/thermal water/air heating  
697 system: A parametric study, Renewable Energy 31 (2006) 2460-2474.
- 698 [59] B. Sandnes, J. Rekstad. A photovoltaic/thermal (PV/T) collector with a polymer† absorber  
699 plate. Experimental study and analytical model, Solar Energy (2002) 63-73.
- 700 [60] H.A. Zondag, D.W. de Vries, W.G.J. van Helden, R.J.C. van Zolingen, A.A. van  
701 Steenhoven, The yield of different combined PV-thermal collector designs, Solar Energy 74  
702 (2003) 253-269.
- 703 [61] H.A. Zondag, D.W. de Vries, W.G.J. van Helden, R.J.C. van Zolingen, A.A. van  
704 Steenhoven, the thermal and electrical yield of a PV-thermal collector, Solar Energy 72 (2002)  
705 113-128,.
- 706 [62] Y. Tripanagnostopoulos, Th. Nousia, M. Souliotis, P. Yianoulis, Hybrid  
707 photovoltaic/thermal solar systems, Solar Energy 72 (2002) 217-234.

- 708 [63] T.T. Chow, Performance analysis of photovoltaic–thermal collector by explicit dynamic  
709 model, *Solar Energy* 75 (2003) 143 – 152.
- 710 [64] Y. Morita, T. Fujisawa, T. Tani, Moment performance of photovoltaic/thermal hybrid panel  
711 (numerical analysis and exergetic evaluation). *IEEJ Transactions on Industry Applications* 199  
712 (1999) 81-87.
- 713 [65] S.A. Kalogirou, Use of TRNSYS for modelling and simulation of a hybrid PV–thermal  
714 solar system for Cyprus. *Renewable Energy* 23 (2001) 247 – 260.
- 715 [66] J. Gao, Y. Zhang, Y. Liu, X. Gao, Study on the temperature variation of the water-cooled  
716 photovoltaic solar template. 2010 International Conference on Intelligent System Design and  
717 Engineering Application, IEEE, Changsha, China, 2010.
- 718 [67] T. Nualboonrueng, P. Tuenpusa, Y. Ueda, A. Akisawa, The performance of PV-T systems  
719 for residential application in Bangkok, *Progress in Photovoltaics* 21 (2013) 1204-1213.
- 720 [68] H.P. Garg, R.K. Agarwal, Some aspects of a PV/T collector/forced circulation flat plate  
721 solar water heater with solar cells. *Energy Conversion and Management* 36 (1995) 87 – 99.
- 722 [69] J. Ji, J. Han, T. Chow, H. Yi, J. Lu, W. He, W. Sun, Effect of fluid flow and packing factor  
723 on energy performance of a wall mounted hybrid photovoltaic/water-heating collector system.  
724 *Energy Build* 38 (2006) 1380 – 1387.

**Highlights**

- The thermal performance of a PV/T module was evaluated by a novel numerical model for a hot climate region.
- The computational time was reduced by applying different thermal boundary conditions on both sides of the PV/T numerical model.
- Three-dimensional temperature distribution of the PV/T module was presented.
- The thermal energy was validated using different values of mass flow rates.

**Tareq Salameh:** Conceptualization, Project administration, Methodology, Funding acquisition, Supervision, Writing - review & editing. **Muhammad Tawalbeh:** Investigation, Validation, Methodology, Formal analysis, Data curation, Writing - original draft. **Adel Juaidi:** Investigation, Methodology, Formal analysis, Writing - review & editing. **Ramez Abdallah:** Investigation, Methodology, Writing - review & editing. **Abdul-Kadir Hamid:** Project administration, Funding acquisition, Supervision, review & editing.

**Declaration of interests**

The authors declare that they have no known competing financial interests or personal relationships that could have appeared to influence the work reported in this paper.

The authors declare the following financial interests/personal relationships which may be considered as potential competing interests:

Journal Pre-proof